Cadherins orchestrate specific patterns of perisomatic inhibition onto distinct pyramidal cell populations

Julie Jézéquel[1,2], Giuseppe Condomitti[1,2], Tim Kroon[1,2], Fursham Hamid[1,2], Stella Sanalidou[1,2], Teresa Garces[1,2], Patricia Maeso[1,2], Maddalena Balia[1,2] & Beatriz Rico[1,2*]

[1]Centre for Developmental Neurobiology, Institute of Psychiatry, Psychology and Neuroscience, King's College London, London SE1 1UL, United Kingdom.

[2]MRC Centre for Neurodevelopmental Disorders, King's College London, London SE1 1UL, United Kingdom.

[*]Corresponding author. Email: beatriz.rico@kcl.ac.uk

Highlights

- Cortical pyramidal cells targeting different brain areas receive a specific ratio of PV+ and CCK+ inhibitory inputs
- Cell type-specific perisomatic inhibition is determined early during postnatal development
- Cdh12 controls CCK+ inhibition onto L5 intracortical pyramidal cells, while Cdh13 regulates PV+ inhibition onto L5 extracortical pyramidal cells
- Pyramidal cells projecting to intra- or extra-cortical areas receive inputs from segregated PV+ cell networks

Summary

In the mammalian neocortex, excitatory pyramidal cells are assembled into distinct subnetworks, which project to different brain areas. GABAergic interneurons were long thought to connect promiscuously and extensively to pyramidal neurons, but recent evidence supports the existence of a cell type-specific inhibitory connectome. How and when interneurons establish such a precise connectivity pattern among intermingled populations of excitatory neurons remains enigmatic. Here, we investigated the molecular rules shaping cell type- and input-specific inhibitory connectivity in different Layer 5 (L5) pyramidal cell populations. We found that neighboring L5 intra- (L5 IT) and extra-telencephalic (L5 ET) neurons receive different combinations of inhibitory perisomatic inputs from Parvalbumin- (PV+) and Cholecystokynine-positive (CCK+) basket cells. We also identified *Cdh12* and *Cdh13*, two cadherin superfamily members, as critical mediators of L5 pyramidal cell type-specific inhibitory connectivity. Our data revealed a minimal overlap between L5 IT and L5 ET presynaptic inhibitory networks, and suggests that different populations PV+ basket cells innervate distinct L5 pyramidal cell types. Altogether, our work unravels the contribution of cadherins in shaping cortical interneuron wiring and provides new insights into the development of inhibitory microcircuits.

Introduction

Precise and fine-tuned neuronal connectivity underlies even the most basic animal behavior. This connectivity reaches an extreme complexity in the mammalian cerebral cortex, where two main types of neurons coexist: glutamatergic principal or pyramidal cells and gamma-aminobutyric acid-expressing (GABAergic) interneurons. Pyramidal cells are highly heterogeneous and are organized into distinct neuronal ensembles, forming unique information-processing streams [1,2]. By selectively targeting different subcellular compartments of principal cells, inhibitory interneurons play a critical role in gating cortical activity and ensuring proper brain computation [3]. However, how interneurons regulate such intricate and diverse excitatory networks remains enigmatic.

The classical vision assumed that interneurons indiscriminately target all pyramidal cells in the cerebral cortex [4–6]. However, there is now substantial evidence indicating that cell type-specific connectivity motifs mediate the wiring of inhibitory connections [7–12]. These studies suggest instead that interneurons discriminate among different postsynaptic targets and exhibit biased connectivity patterns [7,8,10,12–15]. For example, pyramidal cells projecting to subcortical areas receive more perisomatic inhibition from parvalbumin-expressing (PV+) basket cells than local-projecting neighboring cells [8,14]. Similarly, cholecystokinin-expressing (CCK+) basket cells preferentially target pyramidal cells sending axons outside the hippocampus [7]. Consequently, interneurons not only influence pyramidal cell activity by targeting different subcellular compartments but can also gate the information flow of distinct subnetworks of pyramidal cells.

How interneurons select specific targets during development and what molecular programs control such refined connectivity motifs to arise is unknown. Here, we took advantage of the stereotypical organization of cortical layer 5 (L5) and the coexistence of two pyramidal cell types with distinct projection targets to explore the emergence and molecular determinants of

cell type-specific perisomatic inhibition. Focusing on L5 intra- (L5 IT) and extra-telencephalic (L5 ET) pyramidal cells [16–20], we demonstrate that these pyramidal cell populations receive different ratios of PV+ and CCK+ inputs. We also found that members of the Cadherin superfamily, *Cdh12* and *Cdh13*, contribute to instructing cell type- and input-specific perisomatic inhibition. Moreover, simultaneous mapping of the inhibitory inputs targeting L5 IT and L5 ET revealed the contribution of different populations of PV+ basket cells to individual pyramidal cells. Altogether, our findings unveil a molecular and cellular code orchestrating the assembly of inhibitory microcircuits targeting different pyramidal cell populations.

Results

Differential perisomatic inhibition onto distinct pyramidal cell types

Previous studies in the hippocampus, entorhinal cortex and prefrontal cortex have shown that the levels of perisomatic inhibition differ between pyramidal cells with distinct projection targets [7–11]. To investigate whether this principle is conserved in other cortical areas, we took advantage of the stereotypical organization of layer L5 in the primary somatosensory cortex (S1), where distinct pyramidal cell types can be segregated based on their axonal projections [16]. In this region, L5 IT neurons send their axons to the contralateral hemisphere and other cortical areas, while L5 ET neurons target subcortical structures, including the thalamus, superior colliculus, and brainstem nuclei [19]. To simultaneously label L5 IT and L5 ET neurons, we co-injected RB488 and RB555 fluorophore-coated latex retrobeads in the contralateral S1 and the ipsilateral pons of wild-type neonates (Figures 1A and S1). We chose cortico-pontine projecting neurons as a reference for L5 ET neurons because early postnatal injections in the pons provided the most reliable labeling among the different subcortical areas tested. Retrograde tracing from the injection sites revealed a stereotypical double-layer cell

distribution (Figure 1A) whereby L5 ET neurons were restricted to L5b while L5 IT cells were enriched in L5a but present across the entire layer (Figure 1A). To determine whether these two populations of neurons receive different levels of perisomatic inhibition, we recorded miniature inhibitory postsynaptic currents (mIPSCs) from neighboring retrogradely labeled S1 L5 IT and L5 ET neurons. Whole-cell voltage-clamp recordings at P30 revealed that the mIPSC frequency was higher in L5 ET than in L5 IT neurons, whereas both cell types exhibited similar mIPSC amplitude (Figure 1B). These results reveal that S1 L5 ET cells receive significantly more inhibitory inputs than L5 IT neurons.

Cell type-specific inhibitory motifs onto pyramidal cell populations

PV+ and CCK+ basket cells are the two major sources of perisomatic inhibition in the cerebral cortex [21,22]. To investigate the contribution of each interneuron population to the perisomatic inhibition of L5 pyramidal neurons, we quantified the density of PV+ and CCK+ synapses onto the soma of L5 IT and L5 ET neurons at P30 using specific presynaptic markers: Synaptotagmin 2-positive (Syt2+) for PV+ inputs [23] and cannabinoid receptor 1 (CBR1) for CCK+ inputs [24]. We found that PV+ boutons were twice more abundant in L5 ET neurons than in L5 IT cells (Figure 1C, and 1D), confirming our functional analysis (Figure 1B). In contrast, L5 IT neurons received more CCK+ boutons labelled with CB1R than L5 ET cells (Figure 1F and 1G). Given that pyramidal cells receive considerably more PV+ than CCK+ inputs ([25] and present study), our mIPSC recordings might mainly reflect PV+ innervation, masking the contribution of CCK+ basket cells (Figure 1B).

We next investigated when these distinct patterns of perisomatic inhibition emerge. To this end, we characterized the developmental timeline of PV+ and CCK+ inputs onto L5 IT and L5 ET neurons. We observed that the differences in PV+ innervation already existed during early stages of synapse formation (P10) and increased throughout postnatal development (Figure

1E). CCK+ inhibition followed a slower progression, although the preferential targeting of L5 IT neurons was already evident by P12 and got gradually more robust over time (Figure 1H). Altogether, our results indicate that PV+ and CCK+ interneurons provide cell type-specific innervation onto neighboring L5 pyramidal cell populations embedded in distinct neuronal networks, and that such connectivity patterns are determined during the early stages of synapse formation.

Cell type-specific transcriptional programs in distinct L5 pyramidal cells

What molecular mechanisms underlie the different innervation patterns of PV+ and CCK+ interneurons? We hypothesized that the postsynaptic targets (i.e. L5 IT and L5 ET neurons) can shape interneuron inputs to match their inhibitory requirements by expressing cell type-specific synaptic programs. We examined the transcriptomic signatures of L5 IT and L5 ET neurons when the differential perisomatic inhibition patterns first emerged to explore whether postsynaptic molecules could instruct cell type-specific levels of perisomatic inhibition. We dissected S1 deep layers at P10 and isolated retrogradely labeled L5 IT and L5 ET neurons using fluorescence-activated cell sorting. We then performed bulk RNA-sequencing (RNAseq) and compared the gene expression profiles of both populations of pyramidal cells (Figure 2A and S2A). Using this approach, we identified multiple cell type-specific genes, including known markers of L5 IT neurons such as *Lmo4* and *Satb2*, and of L5 ET cells like *Bcl11b* and *Crym* (Figure S2B). Although astroglia or oligodendroglia genes were absent from our dataset, we unexpectedly found some microglial genes in the L5 ET population (Figure S2C). To enrich our study with L5-specific genes, we used bioinformatics to intersect our dataset with two other RNA-seq datasets [26,27] (Figure 2B and S2D). In brief, genes differentially expressed (DEGs) in our dataset and in [26] were filtered for neonatal-regulated genes [27]. A final list of DEGs was then identified by combining: (1) the two studies (130 DEG), (2) the present study only (342 DEG),

and (3) Klingler et al., 2019 only (381 DEG) (Figure 2C). Following this criterion, we obtained 853 DEG between L5 IT and L5 ET neurons (Figure 2C-2E, S2E and S2F). Gene Ontology (GO) analysis of this restricted dataset unveiled an enrichment in genes involved in the organization and function of the synapse (Figure 2E). L5 IT-enriched genes contributed to a higher proportion of these synaptic GO terms, but terms relevant to perisomatic inhibition such as "GABAergic synapse" and "cell-cell adhesion" also featured in the analysis were equally represented in L5 IT and L5 ET cells (Figure S2E).

Several families of cell-surface molecules have been implicated in cell-cell type recognition during neural circuit development [28–31]. We then curated the DEGs list for genes coding cell-surface molecules to identify candidate genes instructing cell type-specific perisomatic inhibition in L5 pyramidal cell populations. Genes were ranked according to the sum of a specificity score measuring the expression of a corresponding cell-surface partner in the preferential presynaptic targeting interneuron (i.e., CCK-L5 IT and PV-L5 ET, Figure 2F) - and the gene expression fold-change score (Figure 2G). Using this set of criteria, two cadherin superfamily members appeared as top candidate genes – Cadherin-12 (*Cdh12*) for L5 IT and Cadherin-13 (*Cdh13*) for L5 ET. To validate our bioinformatic predictions, we performed single-molecule RNA fluorescent in situ hybridization and measured *Cdh12* and *Cdh13* transcript levels in both populations of L5 pyramidal neurons at P10 (Figure S3). We retrogradely labeled L5 IT and L5 ET neurons in these experiments using adeno-associated viruses (AAVs) expressing tag-BFP or tdTomato, respectively (Figure S3A). *Cdh12* RNA expression was three times more enriched in L5 IT than L5 ET neurons (Figure S3B and S3C). Conversely, *Cdh13* RNA was twice more abundant in L5 ET neurons than in L5 IT neurons (Figure S3D and S3E). These findings reveal that L5 IT and L5 ET express a unique cadherin signature, which mirrors cell type-specific PV+ and CCK+ basket cell connectivity motifs onto L5 pyramidal cell populations.

Cell type- and input type-specific inhibition of pyramidal cell populations require *Cdh12* and *Cdh13*

To assess whether postsynaptic *Cdh12* and *Cdh13* play a role in instructing CCK+ and PV+ basket cell inputs in the two populations of pyramidal cells, we performed cell type-specific loss-of-function experiments using a conditional knockdown (KD) strategy *in vivo* [32]. We designed Cre-dependent AAVs expressing short-hairpin RNAs against control (*shLacZ*) and our candidate genes (*shCdh12* and *shCdh13*) and confirmed their efficiency *in vitro* (Figure S4A, S4B). To specifically down-regulate the expression of our candidate genes in L5 IT neurons (Figure 3A), we used the *Tlx3-Cre* mouse line, which labels these cells [33]. To target L5 ET cells, we injected a retrograde Cre-expressing AAV virus (*rAAV2retro-Cre*) in the pons of wild-type mice. In both cases, we injected Cre-dependent *shCdh12* and *shCdh13* AAV in S1 (Figure 3E). We confirmed the efficiency of both approaches to down-regulate the expression of *Cdh12* and *Cdh13 in vivo* (Figure S4C-S4F) and quantified the density of PV+ and CCK+ inputs on the somas of L5 IT and L5 ET neurons at P30. We found that *Cdh12* KD did not impact the PV+ innervation of L5 IT neurons (Figure 3B-3C). In contrast, *Cdh12* KD significantly reduced CCK+ inputs onto L5 IT cells, which remained unaffected following *Cdh13* KD (Figure 3B and 3D). Conversely, *Cdh13* KD reduced the number of PV+ inputs targeting L5 ET neurons without affecting the CCK+ inhibition (Figure 3F-3H). Consistent with these observations, we found that the *Cdh13* KD reduced mIPSCs frequency in L5 ET neurons (Figure S5). *Cdh12* KD did not reveal changes in mIPSCs frequencies in L5 IT neurons (Figure S5), which may be explained by the small contribution of CCK+ inputs compared to PV+ inputs to the total inhibition received by these cells. Surprisingly, *Cdh12* KD did not impact CCK+ inputs targeting L5 ET neurons, and *Cdh13* KD did not modify PV+ inhibition in L5 IT pyramidal cells (Figure 3B, 3C, 3F and 3H), which suggests a cell type-specific role

for *Cdh12* and *Cdh13* in the wiring of CCK+ and PV+ inputs. Interestingly, our results also revealed that reducing PV+ or CCK+ inputs in L5 pyramidal cells does not trigger an apparent compensation from the other inhibitory source. This observation is consistent with the idea that these two types of interneurons play different roles in modulating the activity of pyramidal cells. Altogether, our findings suggest that *Cdh12* expression in L5 IT neurons instructs CCK+ innervation, whereas *Cdh13* expression in ET neurons recruits PV+ inputs.

Mapping pyramidal cell populations inhibitory connectivity

Our previous experiments revealed that *Cdh12* and *Cdh13* down-regulation does not affect perisomatic inputs in the same way in the two populations of L5 pyramidal cells (Figure 3). This suggests that the same molecule, expressed in different cell types, may not instruct the same connectivity motifs. A plausible hypothesis is that distinct molecular codes exist for each population of pyramidal cells because interneuron populations are also diverse. Consistent with this notion, interneurons diversity is extensive and several subtypes of PV+ and CCK+ basket cells have been identified based on their morphological, electrophysiological and transcriptomic (MET-types) signatures [34]. We thus hypothesized that different subtypes of PV+ and CCK+ interneurons innervate L5.

To test this hypothesis, we engineered a multiplex rabies-based monosynaptic tracing approach [35,36] to delineate the cell type-specific inhibitory input maps of each population of L5 pyramidal cells (Figure 4A). In these experiments, we focused on PV+ basket interneurons because they represent the most abundant source of perisomatic inhibition in the cerebral cortex [37–40]. Multiplex monosynaptic tracing relies on specific rabies viral envelopes (EnvX) and their corresponding receptors (TVX). To simultaneously visualize presynaptic networks of L5 IT and L5 ET neurons, we designed distinct *EnvA/TVA* and *EnvB/TVB* complexes and employed two recombinase systems to selectively target L5 IT and L5 ET cells in the same animal (Figure

5A). We injected a *FlpO*-expressing retrograde AAV in the pons of *Tlx3-Cre* mice; hence neighboring L5 ET and L5 IT neurons would express *FlpO* and *Cre*, respectively (Figure 4A-4C). We injected Flp- and Cre-dependent viruses in S1 to obtain cell type-specific receptor expression. To target L5 ET neurons, we injected two *FlpO*-dependent AAVs, one encoding a mutant TVA and a membrane-bound GFP and another encoding the RV glycoprotein *oG* (Figure 4A-4D). We then injected *Cre*-dependent AAVs expressing a BFP-tagged TVB and *oG* to target L5 IT cells (Figure 4A-4D). Three weeks post-injections, we injected two distinct rabies into S1, one encoding G-deficient EnvA and tdTomato and another encoding G-deficient EnvB and nuclear GFP (Figure 4A-4G and S7). This combination allowed retrograde monosynaptic tracing and visualization of inputs in both populations of L5 pyramidal cells, which we examined after the rabies injection.

We observed that L5 IT starter cells (expressing BFP and nuclear GFP) were mainly located in L5a (Figure 4C and 4E) whereas L5 ET starter cells (expressing membrane-bound GFP and cytosolic tdTomato) were restricted to L5b (Figure 4C and 4F). It is worth mentioning that the two recombination systems used in this approach are not equally efficient because *Cre* expression was achieved in virtually all L5 IT neurons *via* the *Tlx3-Cr*e mouse line, while variable *Flp* viral copies were expressed in a fraction of L5 ET cells. We consistently observed more L5 IT starter cells than L5 ET starter cells (Figure 4E, 4F and 4H). Nevertheless, the total number of inputs reaching each L5 pyramidal cell type was comparable (Figure 4H), validating our experimental approach. Furthermore, we did not observe any labeled cells in wild-type mice, further confirming the specificity of our method (Figure S6). We then mapped the afferent connections of L5 IT and L5 ET starter cells throughout the neocortex. In each brain, we quantified the number of inputs for each L5 pyramidal cell type as a fraction of the total number of inputs in the entire neocortex (Figure 4I). We observed that the number of inputs per starter cell was much higher for L5 ET neurons than L5 IT cells (Figure 4J), consistent with

other studies showing that L5 ET neurons receive more neuronal connections than L5 IT neurons [41].

To compare the fraction of inhibitory inputs onto both L5 pyramidal cell populations, we then quantified the proportion of PV+ inputs over the total number of inputs in the neocortex (Figure 5A-5C). We found that the fraction of PV+ input cells targeting L5 ET neurons was significantly higher than in L5 IT cells (Figure 5B). These results were consistent with our synaptic analysis and confirmed that L5 ET neurons receive more PV+ inputs from more PV+ cells than L5 IT neurons. We also examined whether the same PV+ basket cells could innervate both populations of L5 pyramidal cells or whether different PV+ cells target specific L5 ET and L5 IT neurons. In the first scenario, we would expect a significant fraction of PV+ cells containing both rabies. Otherwise, most PV+ cells should only express nuclear GFP or tdTomato. We found a minimal fraction of double-labeled afferent PV+ cells (Figure 5A, 5B and 5D), demonstrating that most PV+ cells innervated either L5 IT neurons or L5 ET cells. The very few PV+ cells contacting both populations of L5 pyramidal cells were primarily allocated in layer 5a (Figure 5E). Moreover, we found that the PV+ interneurons contacting L5 IT and L5 ET cells have distinct laminar distributions (Figure 5E). We observed that PV+ interneurons projecting to L5 IT neurons were spread across L2/3, L4 and L5a, while L5 ET neurons primarily received local inhibition from L5a and L5b PV+ cells (Figure 5E). In sum, our experiments suggest that L5 IT and L5 ET neurons receive inhibition from segregated presynaptic networks of PV+ cells.

Based on these findings, we hypothesized that different interneuron types may target specific populations of pyramidal cells by expressing matching molecular programs. To address this question, we analyzed *Cdh13* expression levels across different types of PV+ interneurons [34]. We found that PV+ cells with their somas or axonal arbor in L5b (*Pvalb-Gabrg1* and *Pvalb-*

Akr1c18-Ntf3) contain the highest levels of *Cdh13* mRNA, whereas L5a PV+ interneurons (*Pvalb-Reln-Tac1* and *Pvalb-Gpr149-Islr*) have the lowest levels of *Cdh13* (Figure 5F and 5G).

In summary, our findings support the notion that perisomatic inhibition targeting different populations of L5 pyramidal cells follows strictly defined rules. Firstly, there is a clear preference for the source of presynaptic inhibitory cells (i.e., PV+ versus CCK+ cells). Secondly, there seems to be a precise allocation of specific subtypes of interneurons (i.e., distinct PV+ MET-types) for each type of L5 pyramidal cell.

Discussion

Understanding the core principles governing neuronal connectivity is essential to identifying the intricate flow of information across neuronal circuits in the cerebral cortex. Cortical interneurons exhibit a remarkable diversity and are critical for sculpting the information conveyed by pyramidal cells. Over the last years, new evidence has transformed our view on inhibition, shifting from promiscuous connectivity [4–6,42] to a precise pattern of interneuron connections whose rules are only beginning to be understood [7–12]. However, how this inhibition emerges and the molecular programs underlying the emergence of precise cell-cell recognition is still unknown. Our study demonstrates that pyramidal cells shape interneuron wiring by expressing specific molecular codes that shape cell type-specific inhibitory connectivity. We found that distinct populations of L5 pyramidal cells promote unique perisomatic inhibitory patterns by expressing two cadherins. *Cdh12* conducts CCK+ inhibition onto L5 IT neurons, and *Cdh13* exclusively controls PV+ inhibition onto L5 ET cells. This differential inhibition pattern is acquired by L5 pyramidal cells during the initial steps of synaptogenesis, suggesting that connectivity features might be intrinsically imprinted during cell type specification.

A cell type-specific code dictates diverse inhibitory inputs onto pyramidal cells

The amount of inhibition received by pyramidal cell correlates with their projection pattern [7–12]. Our findings demonstrate that this rule is conserved across different cortices, revealing a consistent preference of L5 IT neurons for CCK+ inputs L5 ET neurons for PV+ inputs in the mouse somatosensory cortex. Among other cell-surface molecules, *Cdh12* and *Cdh13* are differentially enriched between these two populations of pyramidal cells. Both cadherins are capable of homophilic interactions [43,44] and show specific expression patterns within the interneuron subtype that match the preferred inhibitory profile of each pyramidal cell. Previous studies suggested that the chemokine Cxcl12 might direct PV+ axons to target L5 ET neurons [45]. While *Cxcl12* was not identified in our RNAseq screening, its low expression in these cells might hinder its detectability.

Even though *Cdh12* and *Cdh1*3 are expressed in both populations of L5 pyramidal cells, they exhibit different functions depending on the cellular context. Indeed, our genetic manipulations demonstrate that *Cdh13* exclusively drives PV+ interneuron wiring onto L5 ET cells, but it does not play a similar role in L5 IT neurons. Conversely, *Cdh12* only drives CCK+ basket connectivity in L5 IT cells despite also being expressed in L5 ET neurons. Why is the role of *Cdh12* and *Cdh13* in instructing CCK+ and PV+ inputs not conserved across different types of L5 pyramidal cells? Cdh13 is an atypical cadherin superfamily member as it lacks a transmembrane domain and is inserted into the plasma membrane via a glycosyl-phosphatidylinositol anchor [46]. As such, Cdh13 requires other proteins for downstream signaling [47] and may interact with different synaptic partners depending on the pyramidal cell type. It is conceivable that L5 IT and L5 ET neurons express different interactomes and may not contain the relevant postsynaptic machinery to allow *Cdh13* and *Cdh12* to instruct PV+ and CCK+ basket cell wiring, respectively. Identifying the co-receptors and downstream signaling mechanisms that regulate cadherin function in this cell type-specific context would shed light on this process.

L5 IT and L5 ET neurons are endowed with segregated inhibitory networks

Trans-synaptic rabies tracing using glycoprotein (G)-deleted rabies virus is a powerful and versatile tool to explore circuit connectivity and uncover the distribution of inputs onto specific neuronal populations [48]. We engineered a multiplex monosynaptic tracing approach to visualize inhibitory inputs onto L5 IT and L5 ET cell types in the same brain, based on previous studies [36,49]. Simultaneous mapping of the presynaptic networks of L5 IT and L5 ET neurons allowed us to examine whether L5 pyramidal cells received inhibition from the same or segregated subtypes of PV+ interneurons. Although our experiments revealed an unbalanced number of starter cells between the two populations of L5 pyramidal cells, we labeled a similar number of inputs for both L5 pyramidal cell types. We found that L5 ET neurons receive a larger fraction of inputs per starter cell than L5 IT cells, reinforcing that L5 ET neurons receive more inhibitory inputs than L5 IT cells and may require more inhibitory control to maintain their excitatory-inhibitory balance.

Our experiments also unveiled that L5 IT and L5 ET neurons received inhibitory inputs from largely segregated presynaptic networks. To our knowledge, such exclusive connectivity patterns have not been described before in the cerebral cortex. Previous studies instead indicate that neighboring cells share inputs [4–6,50]. Our results suggest that such connections are rare and that L5 IT and L5 ET neurons participate in separate networks. It should be noted, however, that the incomplete mapping of all inhibitory inputs to all L5 pyramidal cells undoubtedly lowered the probability of identifying PV+ interneurons connected to both L5 IT and L5 ET neurons. Nevertheless, the different spatial distribution of L5 IT and L5 ET PV+ inputs and the diverse expression patterns of *Cdh13* among different PV+ types strongly suggest that segregated PV-to-pyramidal cell type connections are a rule of inhibitory connectivity in the cerebral cortex, at least for L5. Another possible caveat of these experiments is the minimal fraction of co-labeled inputs compared to single-labeled inputs, which may arise from the

competition of distinct rabies types and jeopardize our capacity to visualize shared inputs. Although we may certainly underestimate the contribution of shared inputs, the fact that we could identify excitatory and inhibitory neurons infected with GFP and tdTomato RV confirms that co-infections are biologically possible in our system. Finally, we cannot exclude the possibility that L5 IT and L5 ET neurons share other types of inputs, although recent work demonstrates that at least some subtypes of somatostatin interneurons also target specific populations of pyramidal cells (Wu et al., 2023).

Previous studies have highlighted the existence of translaminar PV+ inhibition in L5 pyramidal cells [51–54]. Our results revealed that L5 ET neurons receive inhibition primarly from local L5 PV+ interneurons, while L5 IT neurons receive inputs from PV+ cells spread across different layers, with similar local and translaminar inhibitory contributions. At least ten PV+ interneuron subtypes with unique transcriptomic profiles and laminar positions have been identified [34]. We found that the expression profile of *Cdh13* in the different subtypes of PV+ interneurons mirrors the spatial distribution of PV+ inputs preferentially targeting L5 ET cells. Hence, the laminar distribution of PV+ inputs targeting L5 IT and L5 ET cells seem to reflect the existence of different inhibitory circuits organized by the expression of matching cell-surface molecules.

Why do L5 IT and L5 ET require different PV and CCK inhibition levels?

Extensive work has demonstrated the dichotomy of PV+ and CCK+ perisomatic inhibition. PV+ basket cells are often described as clockworks for cortical network oscillations, whereas CCK+ basket cells are seen as modulators of such activity [22,57]. Both basket cells exhibit different intrinsic properties and fire in different phases of behavioral activity [58], but some studies suggest that the function of these interneurons is interlinked. Experience-dependent or experimentally-induced changes in the activity of pyramidal cells cause bidirectional changes

in persisomatic inhibition in the hippocampus [59,60] Specifically, increased activity in pyramidal cells enhances PV-mediated inhibition and reduces CCK-mediated inhibition [59,60]. Here, we found no interdependency between both types of perisomatic inhibition, at least at the input level. Modifying the density of one input – by interfering with *Cdh12* or *Cdh13* levels - did not impact the other, supporting the idea that PV+ and CCK+ basket cells have non-overlapping functions. Our results also suggest that different regulatory mechanisms control the development of the inhibitory wiring and the plasticity of pyramidal neurons.

Why would some neurons need both types of inhibition while others receive barely any CCK+ inhibition? The two populations of L5 pyramidal cells consistently exhibit distinct functions across the different cortical areas. For example, L5 ET neurons exhibit higher contrast sensitivity and broader tuning response than L5 IT neurons [61]. During the early phases of a task, L5 IT cells are actively involved, whereas L5 ET neurons become increasingly recruited in the sensory, motor, and prefrontal cortices as the task progresses [1,62–64]. Evidence also supports the notion that L5 IT neurons uphold and enhance the computational efficiency of all cortical neurons by continuously updating them. In contrast, L5 ET neurons serve as information broadcasters, relaying the updated information to subcortical structures [65]. Our work shows that each population of L5 pyramidal cells receives a different combination of perisomatic inputs. L5 ET cells receive dense and almost exclusively PV+ innervation, whereas both PV+ and CCK+ cells contribute to the perisomatic inhibition of L5 IT cells. Since L5 ET neurons send their outputs outside the cortex, these cells might need tighter regulation. Indeed, mice demonstrate a more adept ability to regulate the activity of ET neurons compared to IT neurons [66]. In contrast, L5 IT cells might compute more diverse information and require increased plasticity [66] CCK+ inputs may confer more precision in the modulation of L5 IT neurons, a phenomenon further reinforced by modulatory pathways [67,68].

Considering the unique function of L5 pyramidal cells, it is foreseeable that any reduction or mistargeting of their inhibitory inputs could significantly disrupt the circuitry, and lead to various pathological conditions [69]. For instance, L5 pyramidal cells seem particularly vulnerable in autism [70,71]. Future investigations to understand the relationship between synaptic excitatory/inhibitory ratio within cortical circuits, input specificity and risk gene expression might shed some light on the etiology of some neurodevelopmental disorders.

Author contributions

Conceptualization, J.J. and B.R.; Methodology, J.J., G.C., T.K., B.R.; Formal Analysis, J.J., T.K., F.H., S.S., M.B.; Investigation, J.J., G.C., T.K., F.H., S.S., T.G., P.M. and M.B.; Resources, B.R.; Writing J.J. and B.R. with inputs from all authors; Visualization, J.J., B.R.; Funding Acquisition, J.J. and B.R.

Acknowledgements

We are thankful to L. Doglio, F. Sanchez-Roman, S. Sanalidou and T. Garces for technical assistance and lab support, and to Ian Andrew for mouse management. The pAAV *hSyn-fDIO-MCS* construct was kindly shared by M. Selten and O. Marín (King's College London) The *pSAD ΔG F3* construct was kindly provided by M. Tripodi (University of Cambridge). B7GG and HEK293-TVA cells were generously shared by T. Karayannis (University of Zurich). The *pSAD ΔG ChR2c::T2A::tdTomato* construct and the *RVdG-EnvA-tdTomato-ChR2* viral preparation were generously shared by K. Conzelmann (Ludwig-Maximilians-University Munich) and A. Delogu (KCL). We thank the IoPPN Genomics & Biomarker Core Facility, the Advanced Cytometry Platform of the Research and Development Department at Guy's and St Thomas' NHS Foundation Trust for their technical advice and assistance on the FACS experiment, and the CRG Genomics Core Facility of Barcelona for conducting RNA sequencing. Finally, we are grateful to O. Marín, J. Burrone, M. Grubb and C. Bernard for critical reading of the manuscript, and to all members of the Rico and Marín laboratories for stimulating discussions and ideas. This project was supported by grants from Wellcome Trust (202758/Z/16/Z) and European Union's Horizon 2020 research and innovation program (AIMS- 2- TRIALS, 777394) to B.R, and the EMBO Long-Term Fellowship to J.J.

Declaration of interests

The authors declare no competing interests.

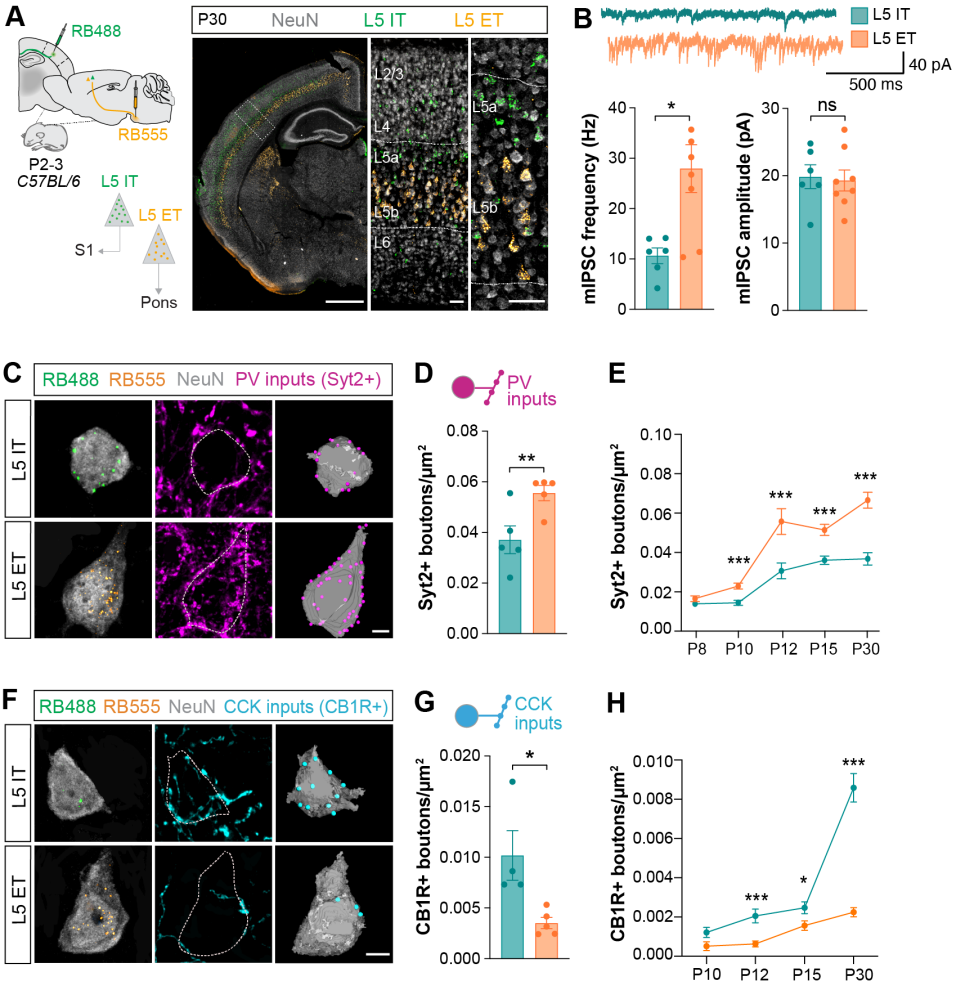
A
RB488
RB555
P2-3
C57BL/6
L5 IT
L5 ET
S1
Pons
P30
NeuN
L5 IT
L5 ET
L2/3
L4
L5a
L5b
L6
B
L5 IT
L5 ET
40 pA
500 ms
mIPSC frequency (Hz)
mIPSC amplitude (pA)
ns
C
RB488 RB555 NeuN PV inputs (Syt2+)
D
PV inputs
Syt2+ boutons/µm²
E
Syt2+ boutons/µm²
P8 P10 P12 P15 P30
F
RB488 RB555 NeuN CCK inputs (CB1R+)
G
CCK inputs
CB1R+ boutons/µm²
H
CB1R+ boutons/µm²
P10 P12 P15 P30

Figure 1

Figure 1. Differential perisomatic inhibition onto distinct pyramidal cell types

(A) Schematic of L5 IT and L5 ET neurons retrograde labelling strategy. Green (RB488) and red (RB555, pseudocolor in orange) fluorescent retrobeads were injected in the contralateral somatosensory cortex (S1) and in the ipsilateral pons of P2-3 C57BL/6J mice to target L5 IT and L5 ET axons, respectively. Retrogradely-labeled L5 IT (green) and L5 ET (orange) cells exhibited a typical double-layered labeling at P30. Pyramidal cell somas were labeled with NeuN. L5 IT neurons were mainly enriched in L5a, while L5 ET were exclusively located in L5b.

(B) Example traces of mIPSCs recorded from retrogradely-labeled L5 IT and L5 ET cells at P30. Quantification of the mIPSCs frequency (Hz) from L5 IT and L5 ET (*L5 IT* n = 6 cells from 3 mice, *L5 ET* n = 8 cells from 2 mice; Mann-Whitney test * $p < 0,05$). Quantification of the mIPSCs amplitude (pA) from L5 IT and L5 ET (*L5 IT* n = 6 cells from 3 mice, *L5 ET*; n = 8 cells from 2 mice; ns, not significant, Mann-Whitney test).

(C) Confocal and 3D-reconstructed images illustrating PV inputs (Syt2+, magenta) onto L5 IT and L5 ET somas labelled with NeuN (grey) and retrobeads.

(D) Quantification of Syt2+ boutons density onto L5 IT and L5 ET at P30 (*L5 IT* n = 5 mice, 62 cells, *L5 ET* n = 5 mice, 92 cells; paired t-test ** $p < 0.01$).

(E) Quantification of Syt2+ boutons density onto L5 IT and L5 ET over post-natal development (*P8 L5 IT* = 60 cells, *L5 ET* = 116 from 5 mice; *P10 L5 IT* = 131 cells, *L5 ET* = 123 cells from 6 mice; *P12 L5 IT* = 103 cells, *L5 ET* = 109 cells from 5 mice; *P15 L5 IT* = 164 cells, *L5 ET* = 125 cells, 7 mice; *P30 L5 IT* = 61 cells, *L5 ET* = 97 cells from 5 mice; multiple t-test Holm-Šídák posthoc, P8 ns, P10 ***$p < 0.001$, P12 **$p < 0.01$, P15 ***$p < 0.001$, P30 *** $p < 0.001$).

(F) Confocal and 3D-reconstructed images illustrating CCK inputs (CB1R+, cyan) onto L5 IT and L5 ET somas labelled with NeuN (grey) and retrobeads at P30.

(G) Quantification of CB1R+ boutons density onto L5 IT and L5 ET at P30 (*L5 IT* n = 4 mice, 82 cells, *L5 ET* n= 5 mice, 83 cells; t-test *p < 0.05).

(H) Quantification of CB1R+ boutons density onto L5 IT and L5 ET over postnatal development (*P10 L5 IT* n = 73 cells, *L5 ET* n = 45 cells from 5 mice; *P12 L5 IT* n = 57 cells, *L5 ET* n = 49 cells from 3 mice; *P15 L5 IT* n= 107 cells, *L5 ET* n = 80 cells, from 5 mice; *P30 L5 IT* n = 127 cells, *L5 ET* n = 120 cells from 5 mice; multiple t-test Holm-Šídák posthoc: P10 ns, P12 *** p < 0.001, P15 * p < 0.05, P30 ***p<0.001)). Data are mean ± SEM, ns, not significant. Scale bars, 500 μm, 50 μm (A) and 5 μm (B, F).

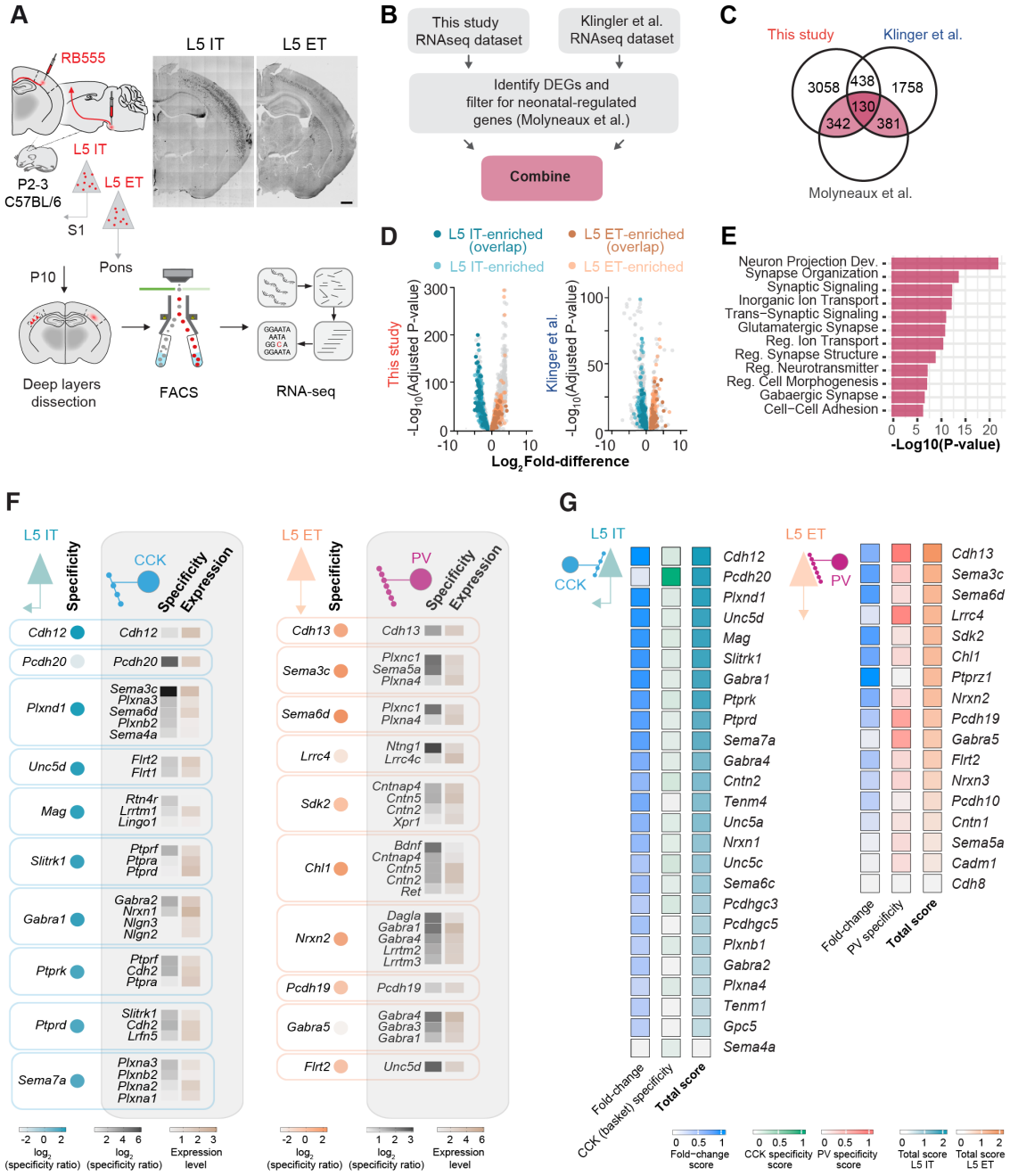
A
RB555
L5 IT
L5 ET
P2-3
C57BL/6
S1
Pons
P10
Deep layers dissection
FACS
RNA-seq
B
This study RNAseq dataset
Klingler et al. RNAseq dataset
Identify DEGs and filter for neonatal-regulated genes (Molyneaux et al.)
Combine
C
This study
Klinger et al.
Molyneaux et al.
3058
438
1758
130
342
381
D
L5 IT-enriched (overlap)
L5 ET-enriched (overlap)
L5 IT-enriched
L5 ET-enriched
This study
Klinger et al.
-Log10(Adjusted P-value)
Log2 Fold-difference
E
Neuron Projection Dev.
Synapse Organization
Synaptic Signaling
Inorganic Ion Transport
Trans−Synaptic Signaling
Glutamatergic Synapse
Reg. Ion Transport
Reg. Synapse Structure
Reg. Neurotransmitter
Reg. Cell Morphogenesis
Gabaergic Synapse
Cell−Cell Adhesion
-Log10(P-value)
F
L5 IT
Specificity
CCK
Specificity
Expression
Cdh12
Pcdh20
Plxnd1
Unc5d
Mag
Slitrk1
Gabra1
Ptprk
Ptprd
Sema7a
L5 ET
PV
Cdh13
Sema3c
Sema6d
Lrrc4
Sdk2
Chl1
Nrxn2
Pcdh19
Gabra5
Flrt2
log2 (specificity ratio)
Expression level
G
L5 IT
CCK
L5 ET
PV
Cdh12
Pcdh20
Plxnd1
Unc5d
Mag
Slitrk1
Gabra1
Ptprk
Ptprd
Sema7a
Gabra4
Cntn2
Tenm4
Unc5a
Nrxn1
Unc5c
Sema6c
Pcdhgc3
Pcdhgc5
Plxnb1
Gabra2
Plxna4
Tenm1
Gpc5
Sema4a
Cdh13
Sema3c
Sema6d
Lrrc4
Sdk2
Chl1
Ptprz1
Nrxn2
Pcdh19
Gabra5
Flrt2
Nrxn3
Pcdh10
Cntn1
Sema5a
Cadm1
Cdh8
Fold-change
CCK (basket) specificity
Total score
PV specificity
Fold−change score
CCK specificity score
PV specificity score
Total score L5 IT
Total score L5 ET

Figure 2

Figure 2. Cell type-specific transcriptional programs in L5 pyramidal cells subpopulations

(A) Schematic of experimental design.

(B) Intersection strategy of our RNAseq dataset with two other studies.

(C) Differentially expressed genes (DEGs) between L5 IT and L5 ET neurons in the three RNAseq datasets.

(D) Volcano plot of DEGs in our study and Klingler et al.

(E) Gene ontology terms significantly enriched in the final dataset.

(F) Cell-specific candidate cell-surface molecules expressed in L5 IT and L5 ET neurons ranked based on their putative pre-synaptic partners' specificity and expression level in CCK basket cells and PV interneurons, respectively. This analysis relies on known protein-protein interactions and gene expression in CCK+ and PV+ cell types described as such, according to (Yao et al., 2021).

(G) Heatmaps showing the fold-change expression, specificity score and resulting total score for L5 IT and L5 ET DEG coding for cell-surface molecules.

Scale bar, 500 μm (A).

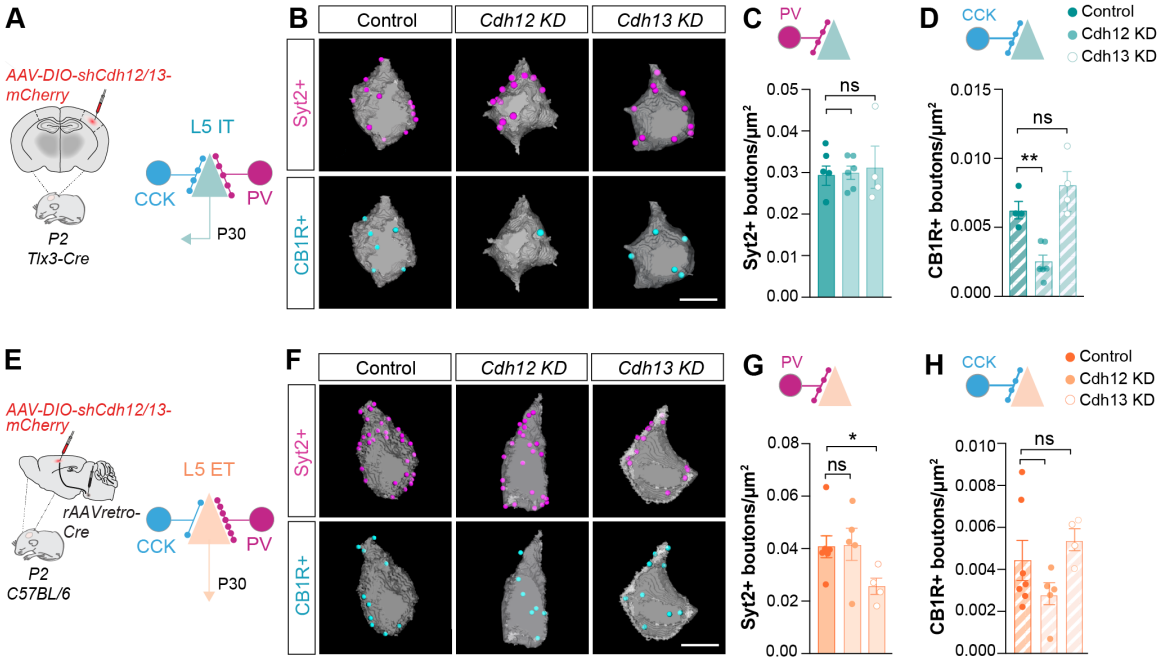
A
AAV-DIO-shCdh12/13-mCherry
P2
Tlx3-Cre
L5 IT
CCK
PV
P30
B
Control
Cdh12 KD
Cdh13 KD
Syt2+
CB1R+
C
PV
ns
Syt2+ boutons/µm²
0.05
0.04
0.03
0.02
0.01
0.00
D
CCK
Control
Cdh12 KD
Cdh13 KD
ns
**
CB1R+ boutons/µm²
0.015
0.010
0.005
0.000
E
AAV-DIO-shCdh12/13-mCherry
rAAVretro-Cre
P2
C57BL/6
L5 ET
CCK
PV
P30
F
Control
Cdh12 KD
Cdh13 KD
Syt2+
CB1R+
G
PV
*
ns
Syt2+ boutons/µm²
0.08
0.06
0.04
0.02
0.00
H
CCK
Control
Cdh12 KD
Cdh13 KD
ns
CB1R+ boutons/µm²
0.010
0.008
0.006
0.004
0.002
0.000

Figure 3

Figure 3. Cadherins drive cell type- and input-specific inhibition onto L5 pyramidal cell subpopulations

(A) Schema of the conditional viral strategy to down-regulate *Cdh12* and *Cdh13* in L5 IT cells and measure its impact on perisomatic inputs at P30.

(B) 3D-reconstructed confocal images of PV+ (Syt2+, magenta) and CCK+ inputs (CB1R+, cyan) onto L5 IT somas.

(C) Quantification of Syt2+ boutons density onto L5 IT (*Control* n = 4 mice, 94 cells; *Cdh12 KD* n = 6 mice, 140 cells; *Cdh13 KD* n = 4 mice, 119 cells; One-way ANOVA ns, Tukey's posthoc: Control vs *Cdh12* KD ns, Control vs *Cdh13* KD ns, *Cdh12* KD vs *Cdh13* KD ns).

(D) Quantification of CB1R+ boutons density onto L5 IT (*Control* n = 4 mice, 95 cells; *Cdh12 KD* n = 6 mice,141 cells; *Cdh13 KD* n = 4 mice, 107 cells; One-way ANOVA ***$p < 0.001$, Tukey's posthoc: Control vs *Cdh12* KD ** $p < 0.01$, Control vs *Cdh13* KD ns, *Cdh12* KD vs *Cdh13* KD *** $p < 0.001$). (E) Conditional viral strategy to down-regulate *Cdh12* and *Cdh13* in L5 ET and the subsequent quantification of perisomatic inputs at P30.

(F) 3D-reconstructed confocal images of PV+ (Syt2+, magenta) and CCK+ inputs (CB1R+, cyan) onto L5 ET somas.

(G) Quantification of Syt2+ boutons density onto L5 ET (*Control* n = 9 mice, 232 cells; *Cdh12 KD* n = 5 mice, 114 cells; *Cdh13 KD* n = 6 mice, 127 cells; One-way ANOVA *$p < 0.05$, Tukey's posthoc: Control vs *Cdh12* KD ns, Control vs *Cdh13* KD * $p < 0.05$, *Cdh12* KD vs *Cdh13* KD * $p < 0.05$).

(H) Quantification of CB1R+ boutons density onto L5 ET (*Control* n = 9 mice, 163 cells); *Cdh12 KD* n = 4 mice (95 cells); *Cdh13 KD* n = 6 mice, 98 cells; One-way ANOVA ns, Tukey's posthoc: Control vs *Cdh12* KD ns, Control vs *Cdh13* KD ns, *Cdh12* KD vs *Cdh13* KD ns). Data are mean ± SEM, ns, not significant. Scale bar, 10μm (B, F).

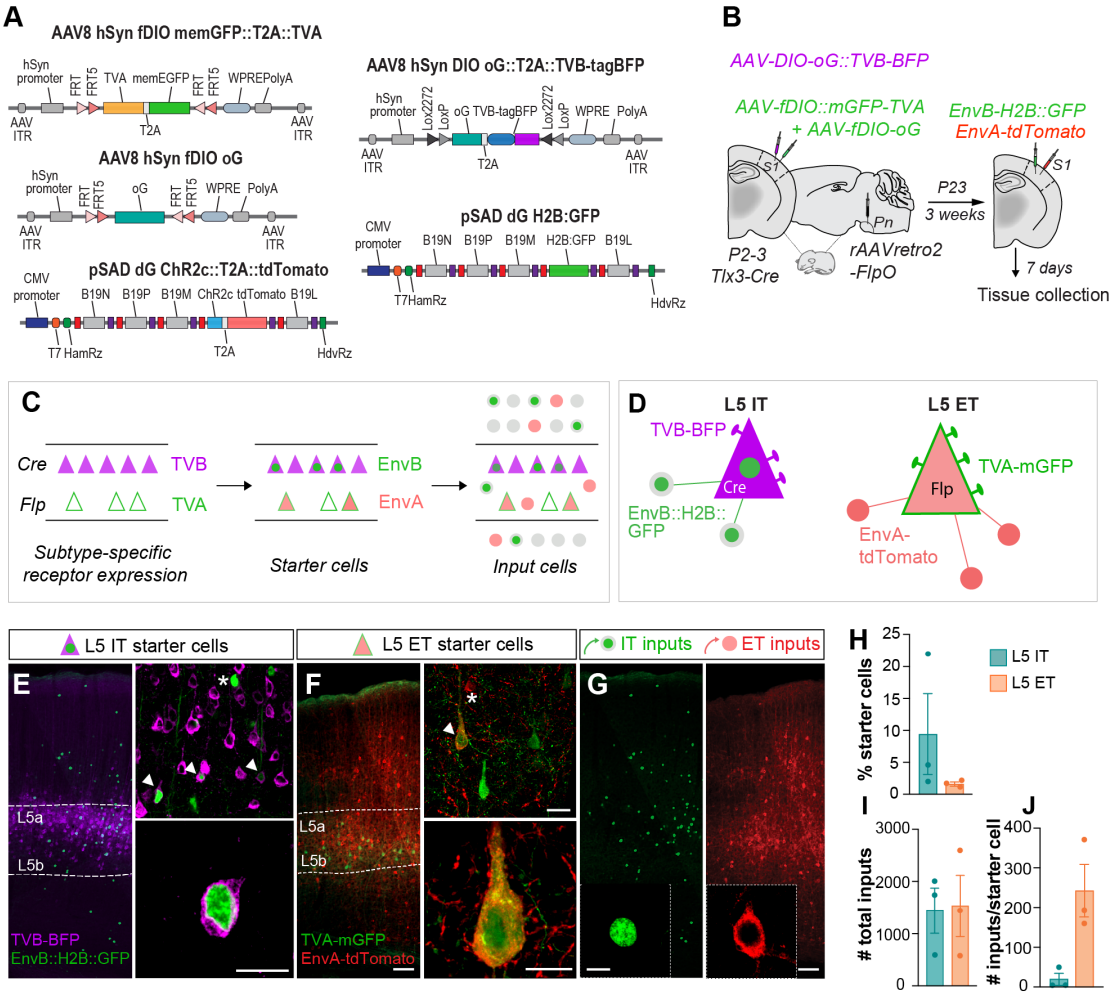
A
AAV8 hSyn fDIO memGFP::T2A::TVA
hSyn promoter
FRT FRT5
TVA
memEGFP
FRT FRT5
WPREPolyA
AAV ITR
T2A
AAV ITR
AAV8 hSyn fDIO oG
hSyn promoter
FRT FRT5
oG
FRT FRT5
WPRE
PolyA
AAV ITR
AAV ITR
pSAD dG ChR2c::T2A::tdTomato
CMV promoter
B19N
B19P
B19M
ChR2c
tdTomato
B19L
T7 HamRz
T2A
HdvRz
AAV8 hSyn DIO oG::T2A::TVB-tagBFP
hSyn promoter
Lox2272 LoxP
oG
TVB-tagBFP
Lox2272 LoxP
WPRE
PolyA
AAV ITR
T2A
AAV ITR
pSAD dG H2B:GFP
CMV promoter
B19N
B19P
B19M
H2B:GFP
B19L
T7HamRz
HdvRz
B
AAV-DIO-oG::TVB-BFP
AAV-fDIO::mGFP-TVA
+ AAV-fDIO-oG
EnvB-H2B::GFP
EnvA-tdTomato
S1
S1
Pn
P23
3 weeks
P2-3
Tlx3-Cre
rAAVretro2
-FlpO
7 days
Tissue collection
C
Cre
TVB
Flp
TVA
EnvB
EnvA
Subtype-specific
receptor expression
Starter cells
Input cells
D
L5 IT
TVB-BFP
Cre
EnvB::H2B::
GFP
L5 ET
TVA-mGFP
Flp
EnvA-
tdTomato
L5 IT starter cells
L5 ET starter cells
IT inputs
ET inputs
E
L5a
L5b
TVB-BFP
EnvB::H2B::GFP
F
L5a
L5b
TVA-mGFP
EnvA-tdTomato
G
H
% starter cells
L5 IT
L5 ET
I
total inputs
J
inputs/starter cell

Figure 4

Figure 4. Mapping pyramidal cell subpopulations inhibitory connectivity

(A) Map of the viral *Cre*- and *FlpO*-dependent oEnvA/oTVA and oEnvB/oTVB constructs.

(B) Schema of the multiplex monosynaptic tracing of L5 IT and L5 ET neurons. A *FlpO*-expressing retrograde AAV was injected into the pons (Pn) of P2-3 *Tlx3-Cre* mice. A cocktail of *Cre*-dependent oG and TVB-BFP expressing AAV, together with *FlpO*-dependent oG and TVA-mGFP AAVs were injected into the S1. Three weeks later, *EnvA-RVΔG-tdTomato* and *EnvB-RVΔG-H2B:GFP* were co-injected into the S1. Mice were perfused seven days post-rabies injections.

(C) Schematic of the spatial distribution of receptor-expressing cells, starter cells and input cells for L5 IT and L5 ET populations. Note that L5 IT cells present in L5a express the *Cre* recombinase and can be infected with the TVB-receptor (magenta triangle) and/or EnvB (green and magenta triangle). On the other hand, L5 ET cells present in L5b express the *FlpO* recombinase and can be infected with the TVA-receptor (green outlined triangle) and/or EnvA (green and red triangle). Inputs from L5 IT (green circle) and L5 ET (red circle) neurons can then be mapped across the different cortical layers.

(D) Schematic representation of L5 IT and L5 ET starter cells and their direct inputs expressing the different viruses.

(E) Confocal images illustrating the spatial distribution of L5 IT starter cells. Top panel: L5 IT starter cells (white arrowhead) co-expressing TVB-BFP (magenta) and EnvB-H2B:GFP (green) were intermingled in L5 with TVB-BFP+ (asterisk) and EnvB-H2B:GFP-expressing cells. Bottom panel: Confocal image illustrating a L5 IT starter cell.

(F) Confocal images illustrating the spatial distribution of L5 ET starter cells. Top panel: L5 ET starter cells (white arrowhead) co-expressing TVA-mGFP (green) and EnvA-tdTomato (red) could be detected in L5b, among TVA-mGFP expressing cells and EnvA-tdtTomato expressing cells (asterisk).

(G) Confocal images illustrating the distribution of L5 IT (green) and L5 ET (red) input cells across a cortical column. L5 IT inputs were labelled with a nuclear GFP while L5 ET inputs expressed a cytosolic tdTomato.

(H) Fraction of L5 IT and L5 ET starter cells (n = 3 mice).

(I) Number of L5 IT and L5 ET total inputs (n = 3 mice).

(J) Number of L5 IT and L5 ET inputs per starter cell (n = 3 mice).

Scale bars, 50 μm (E, F, G), 25 μm (E, F), 5 μm (G).

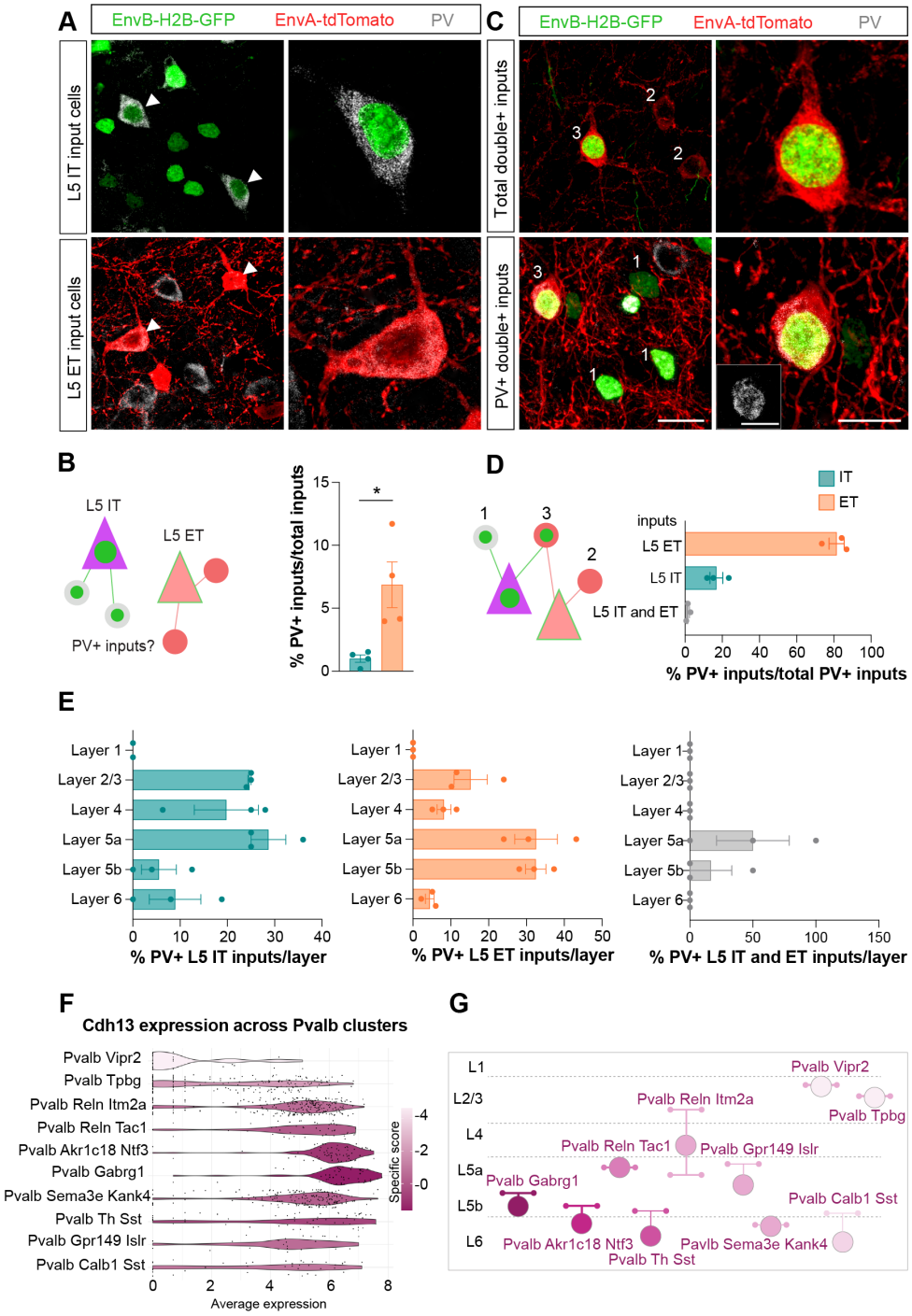
A
EnvB-H2B-GFP
EnvA-tdTomato
PV
L5 IT input cells
L5 ET input cells
C
Total double+ inputs
PV+ double+ inputs
B
L5 IT
L5 ET
PV+ inputs?
% PV+ inputs/total inputs
D
IT
ET
inputs
L5 ET
L5 IT
L5 IT and ET
% PV+ inputs/total PV+ inputs
E
Layer 1
Layer 2/3
Layer 4
Layer 5a
Layer 5b
Layer 6
% PV+ L5 IT inputs/layer
% PV+ L5 ET inputs/layer
% PV+ L5 IT and ET inputs/layer
F
Cdh13 expression across Pvalb clusters
Pvalb Vipr2
Pvalb Tpbg
Pvalb Reln Itm2a
Pvalb Reln Tac1
Pvalb Akr1c18 Ntf3
Pvalb Gabrg1
Pvalb Sema3e Kank4
Pvalb Th Sst
Pvalb Gpr149 Islr
Pvalb Calb1 Sst
Specific score
Average expression
G
L1
L2/3
L4
L5a
L5b
L6
Pvalb Vipr2
Pvalb Reln Itm2a
Pvalb Tpbg
Pvalb Reln Tac1
Pvalb Gpr149 Islr
Pvalb Gabrg1
Pvalb Calb1 Sst
Pvalb Akr1c18 Ntf3
Pvalb Th Sst
Pavlb Sema3e Kank4

Figure 5

Figure 5. Different PV+ subtypes innervate L5 IT and L5 ET pyramidal cell types

(A) Confocal images illustrating L5 IT (green) and L5 ET (red) input cells positive for PV staining (grey). PV+ input cells are indicated with a white triangle.

(B) Fraction of PV+ inputs among L5 IT and L5 ET input cells (n = 3 mice).

(C) Confocal images illustrating L5 IT (type 1, EnvB-H2B:GFP) L5 ET (type 2, EnvA-tdTomato) or input cells infected with the two rabies types (type 3, green and red). A minimal fraction of input cells infected with EnvA and EnvB rabies were also positive for PV (grey).

(D) Proportion of PV+ inputs among L5 IT, L5 ET or L5 IT/ET inputs (n = 3 mice).

(E) Proportion of PV+ inputs per layer for L5 IT, L5 ET and L5 IT/ET inputs (n = 3 mice). (

F) Violin plot of *Cdh13* RNA expression and specificity score across the different PV+ MET-types described by the Allen Brain Atlas (Gouwens et al., 2020).

(G) Schematic laminar distribution of the different PV+ MET-types color-coded for *Cdh13* expression levels.

Scale bars, 20µm (A, C), 10µm (A, C).

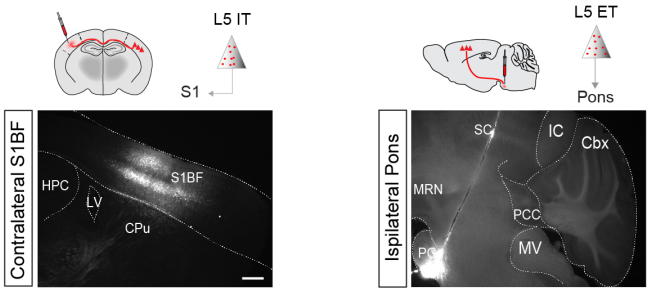
L5 IT
S1
Contralateral S1BF
HPC
LV
S1BF
CPu
L5 ET
Pons
Ispilateral Pons
SC
IC
Cbx
MRN
PCC
MV
PC

Figure S1

Figure S1 (related to Figure 1). Retrobeads injection site

Confocal images of retrobeads injection site in the barrel field area of the somatosensory cortex and in the pons to target L5 IT and L5 ET neurons, respectively. Scale bar, 500μm

A

samples	reads	% uniq mapped	detected genes	% mRNA	% junctions
L5 IT 1	140 182 987	84.9	22 108	73.7	47.0
L5 IT 2	129 784 379	87.3	22 450	73.5	50.4
L5 IT 3	145 713 901	87.4	22 190	73.7	51.3
L5 ET 1	133 762 013	86.0	21 626	74.8	51.5
L5 ET 2	131 227 323	89.5	22 528	73.5	50.5
L5 ET 3	131 233 918	88.6	22 011	73.8	52.5

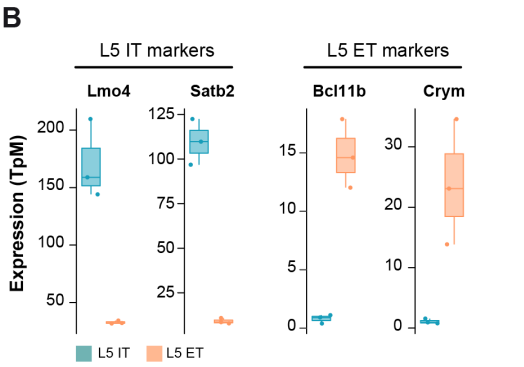

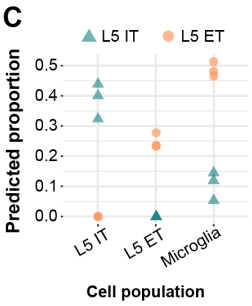

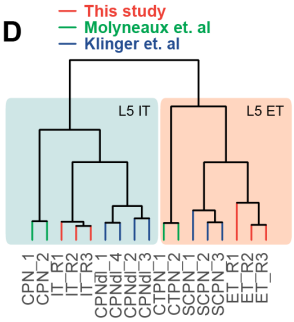

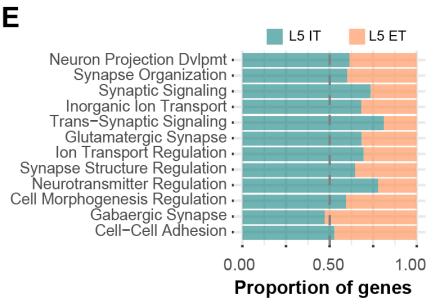

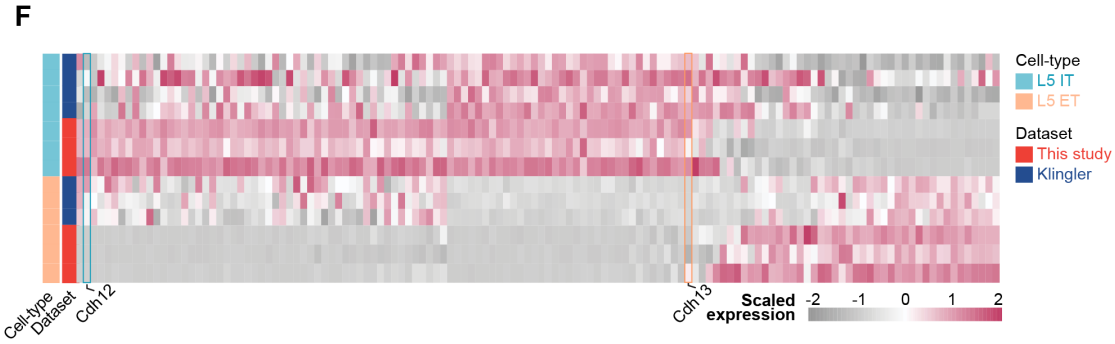

Figure S2

Figure S2 (related to Figure 2). RNA-sequencing data

(A) FastQC analysis of RNA sequencing data for each experimental replicate showing the total number of reads and the percentage of reads uniquely mapped to the reference genome, number of detected genes, mRNA representation and reads mapped to exon-exon junctions.

(B) Expression levels (TpM) of key markers genes in L5 IT and L5 ET pyramidal cell-types.

(C) Estimated cell-type proportions (L5 IT, L5 ET and microglia) after deconvolution of our RNAseq dataset. L5 IT replicates are denoted as triangles, while L5 ET replicates are denoted as dots.

(D) Dendrogram of this study, Molyneaux et al., and Klinger et al., with branches annotated by experimental replicate and L5 pyramidal cell-types. Note the low distance among replicates and how samples cluster by L5 pyramidal cell-type.

(E) Proportion of gene ontology terms enriched in L5 IT or L5 ET cell-types.

(F) Heatmap showing DEG between L5 IT and L5 ET neurons in this study and Klingler et al.

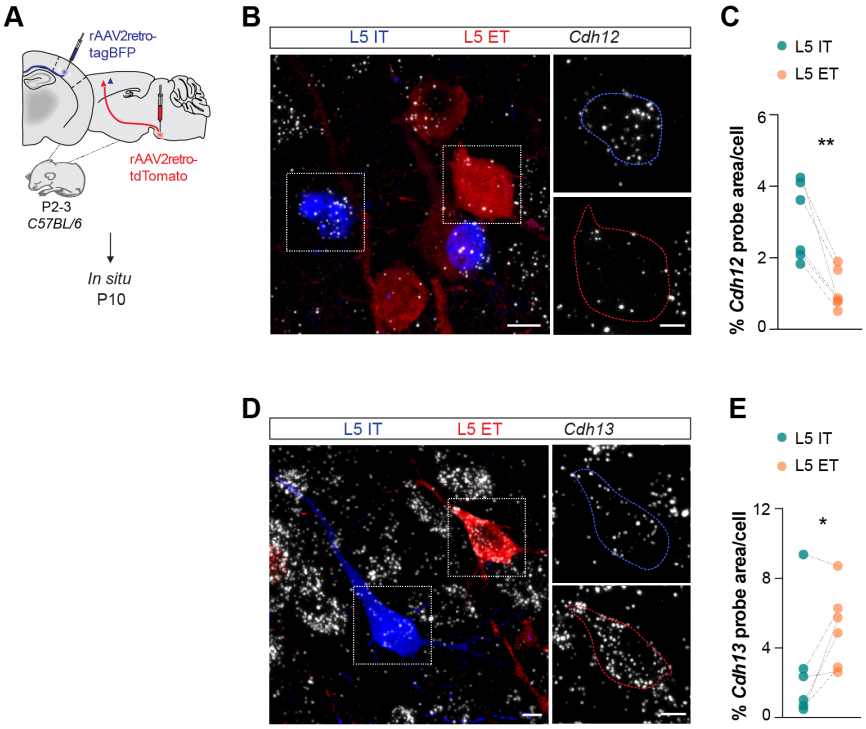
A
rAAV2retro-
tagBFP
rAAV2retro-
tdTomato
P2-3
C57BL/6
In situ
P10
B
L5 IT
L5 ET
Cdh12
C
L5 IT
L5 ET
% Cdh12 probe area/cell
6
4
2
0
**
D
L5 IT
L5 ET
Cdh13
E
L5 IT
L5 ET
% Cdh13 probe area/cell
12
8
4
0
*

Figure S3

Figure S3 (related to Figure 2). *In situ* validation of candidate genes enrichment in L5 IT and L5 ET neurons

(A) Schematic of the experimental design. *rAAVretro2-tagBFP* was injected in the contralateral S1 to target L5 IT cells, *rAAVretro2-tdTomato* was injected in the pons to label L5 ET cells in wildtype mice. Single-molecule fluorescent i*n situ* hybridization was performed at P10 to quantify candidate genes mRNA expression levels.

(B) Confocal images illustrating *Cdh12* RNA expression in retrogradely-labeled L5 IT (blue) and L5 ET (red) neurons.

(C) Fraction of *Cdh12* probe area normalized per cell area (*L5 IT* and *L5 ET* n = 6 mice; paired t-test $^{**}p < 0.01$).

(D) Confocal images illustrating *Cdh13* RNA expression in retrogradely-labeled L5 IT (blue) and L5 ET (red) neurons.

(E) Fraction of *Cdh13* probe area normalized per cell area (*L5 IT* and *L5 ET* n = 6 mice; paired t-test $^{*}p < 0.05$).

Data are mean ± SEM. Scale bars, 5 μm, 10 μm (B, D).

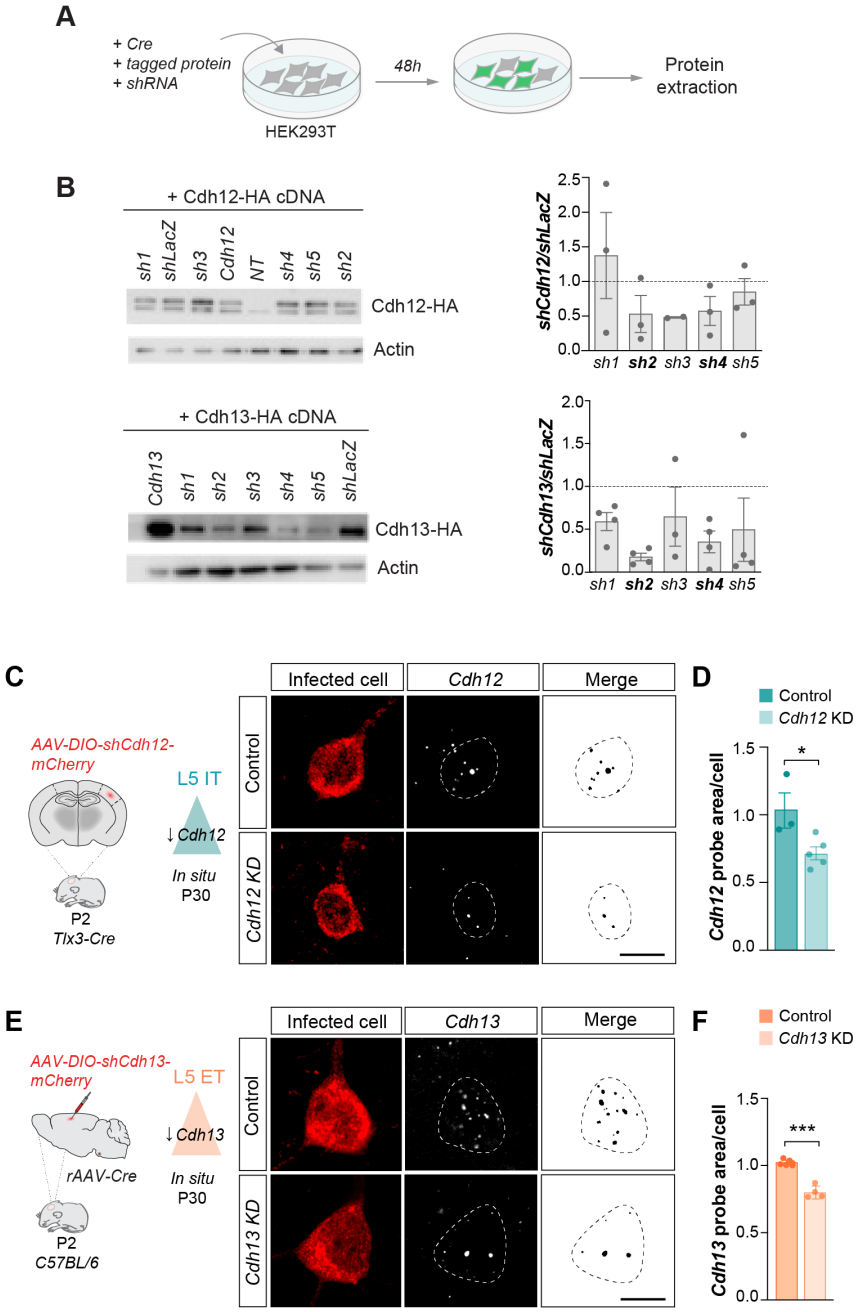
A
+ Cre
+ tagged protein
+ shRNA
HEK293T
48h
Protein extraction
B
+ Cdh12-HA cDNA
sh1
shLacZ
sh3
Cdh12
NT
sh4
sh5
sh2
Cdh12-HA
Actin
shCdh12/shLacZ
sh1 sh2 sh3 sh4 sh5
+ Cdh13-HA cDNA
Cdh13
sh1
sh2
sh3
sh4
sh5
shLacZ
Cdh13-HA
Actin
shCdh13/shLacZ
sh1 sh2 sh3 sh4 sh5
C
AAV-DIO-shCdh12-mCherry
L5 IT
↓Cdh12
In situ
P30
P2
Tlx3-Cre
Infected cell
Cdh12
Merge
Control
Cdh12 KD
D
Control
Cdh12 KD
Cdh12 probe area/cell
E
AAV-DIO-shCdh13-mCherry
L5 ET
↓Cdh13
rAAV-Cre
In situ
P30
P2
C57BL/6
Infected cell
Cdh13
Merge
Control
Cdh13 KD
F
Control
Cdh13 KD
Cdh13 probe area/cell

Figure S4

Figure S4 (related to Figure 3). *In vitro* selection of shRNA and *in vivo* validation of *Cdh12* and *Cdh13* down-regulation

(A) Schema of the experimental design. HEK293T cells were transfected with a cocktail of a Cre-expression plasmid, HA-tagged *Cre*-dependent *Cdh12* and *Cdh13* constructs and plasmids expressing *shRNAs* against the candidate genes. Plasmid expression was visible 48 hours post-transfection, and cells were harvested for protein extraction.

(B) Left: *in vitro* protein expression assessed by Western blot of *Cdh12* and *Cdh13* HA-tagged constructs from transfected HEK923T cells. Right: Quantification of protein signal normalized to actin for each *shRNA*, relative to control transfections with a *shLacZ*-expressing plasmid (n = 3 independent cultures).

(C) Representative confocal images of *Cdh12* RNA expression (white) at P30 in L5 IT cells infected with control *shLacZ*- or *shCdh12*-mCherry (red).

(D) Normalized *Cdh12* RNA expression in L5 IT (*Control* n = 3 mice; *Cdh12 KD* n = 5 mice; one-tailed t-test *$p < 0.05$). (E) Representative confocal images of *Cdh13* RNA expression (white) at P30 in L5 ET cells infected with control *shLacZ*- or *shCdh13*-mCherry (red).

(F) Normalized *Cdh13 RNA* expression in L5 ET (*Control* n = 5 mice, *Cdh13 KD* n = 4 mice, one-tailed t-test ***$p < 0.001$).

Data are mean ± SEM. Scale bar, 10μm (C, D).

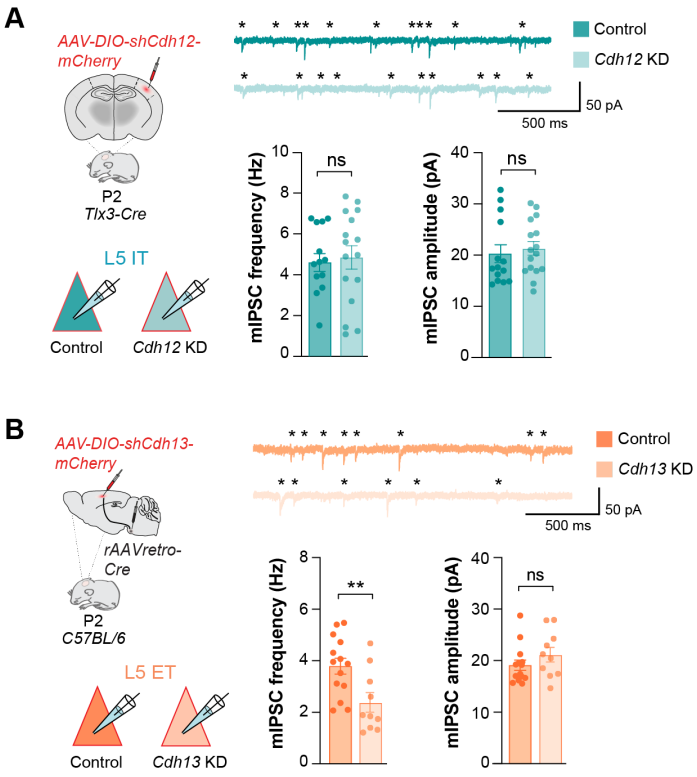
A
AAV-DIO-shCdh12-mCherry
P2
Tlx3-Cre
L5 IT
Control
Cdh12 KD
Control
Cdh12 KD
50 pA
500 ms
mIPSC frequency (Hz)
ns
mIPSC amplitude (pA)
ns
B
AAV-DIO-shCdh13-mCherry
rAAVretro-Cre
P2
C57BL/6
L5 ET
Control
Cdh13 KD
Control
Cdh13 KD
50 pA
500 ms
mIPSC frequency (Hz)
**
mIPSC amplitude (pA)
ns

Figure S5

Figure S5 (related to Figure 3). Functional synaptic outcome of *Cdh12* KD in L5 IT neurons and *Cdh13* KD in L5 ET neurons

(A) Left: Experimental design to selectively down-regulate *Cdh12* in L5 IT and record from control or *Cdh12* KD infected cells. Top: Example traces of mIPSCs recorded from L5 IT cells infected with a control *shLacZ* or *shCdh12*. Bottom: Quantification of the frequency (left) and amplitude (right) of mIPSCs from L5 IT cells in both conditions (*Control* n = 14 cells from 5 mice, *Cdh12 KD* n = 16 cells from 5 mice; t-test frequency and amplitude ns).

(B) Left: Experimental design to selectively down-regulate *Cdh13* in L5 ET and record from control or *Cdh13* KD infected cells. Top: Example traces of mIPSCs recorded from L5 ET cells infected with a control *shLacZ* or *shCdh13*. Bottom: Quantification of the frequency (left) and amplitude (right) of mIPSCs from L5 ET cells in both conditions (*Control* n = 14 cells from 4 mice, *Cdh13 KD* n = 10 cells from 4 mice), t-test frequency $^{**}p < 0.01$, amplitude Mann-Whitney test ns).

Data are mean ± SEM, ns, not significant.

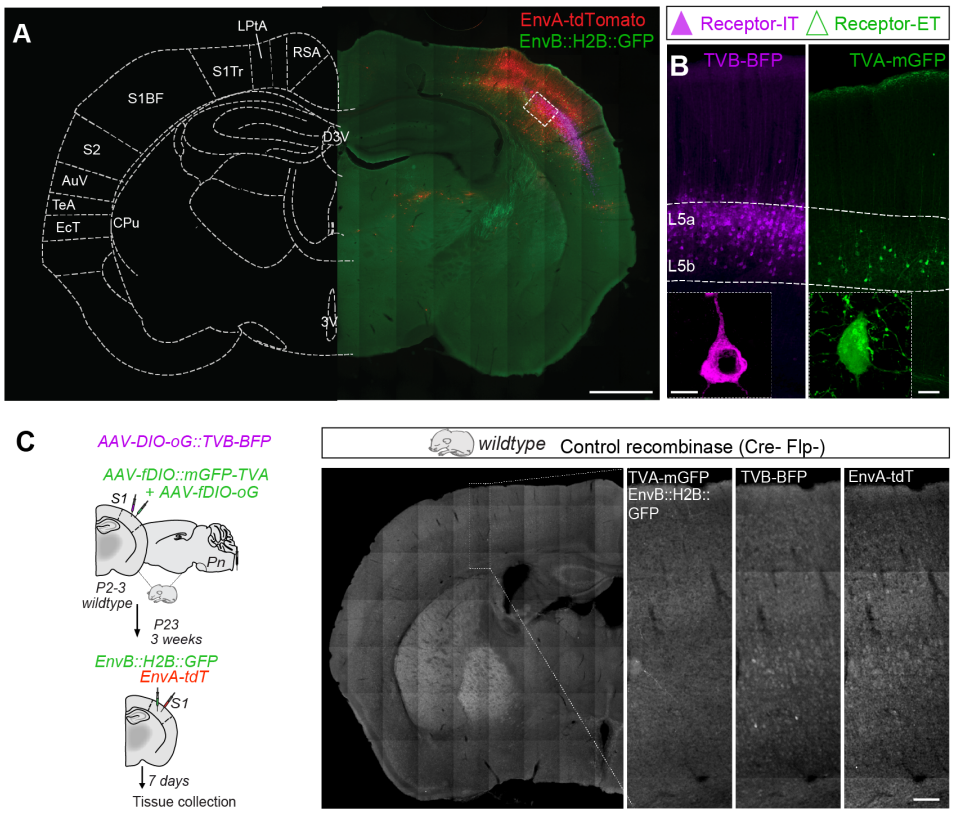
A
LPtA
RSA
S1Tr
S1BF
S2
AuV
TeA
EcT
CPu
D3V
3V
EnvA-tdTomato
EnvB::H2B::GFP
Receptor-IT
Receptor-ET
B
TVB-BFP
TVA-mGFP
L5a
L5b
C
AAV-DIO-oG::TVB-BFP
AAV-fDIO::mGFP-TVA
+ AAV-fDIO-oG
S1
Pn
P2-3
wildtype
P23
3 weeks
EnvB::H2B::GFP
EnvA-tdT
S1
7 days
Tissue collection
wildtype
Control recombinase (Cre- Flp-)
TVA-mGFP
EnvB::H2B::
GFP
TVB-BFP
EnvA-tdT

Figure S6

Figure S6 (related to Figures 4 and 5). Cell type-specific expression of the multiplex monosynaptic tracing strategy

(A) Coronal section depicting TVA/TVB-expressing AAVs and EnvA/EnvB-expressing RV injection sites.

(B) Confocal images illustrating the distribution of L5 IT and L5 ET receptor-expressing cells. L5 IT neurons expressing TVB-BFP (magenta) were mainly present in L5a, while L5 ET expressing TVA-mGFP (green) were exclusively found in L5b.

(C) Following the same strategy, all viruses were injected into a wildtype mouse. Right: Confocal images illustrating the absence of receptor- or RV-infected cells in a Cre- and Flp-negative brain.

Scale bars, 500μm (A) 50 μm (B, C), 10 μm (B).

References

1. Mohan H, An X, Xu XH, et al. Cortical glutamatergic projection neuron types contribute to distinct functional subnetworks. *Nat Neurosci*. 2023;26(March). doi:10.1038/s41593-022-01244-w
2. Kampa BM, Letzkus JJ, Stuart GJ. Cortical feed-forward networks for binding different streams of sensory information. *Nat Neurosci*. 2006;9(12):1472-1473. doi:10.1038/nn1798
3. Wang X., Tegnér J, Constantinidis C, Goldman-Rakic PS. Division of labor among distinct subtypes of inhibitory neurons in a cortical microcircuit of working memory. *Proc Natl Acad Sci U S A*. 2004;101(5).
4. Packer AM, Yuste R. Dense, unspecific connectivity of neocortical parvalbumin-positive interneurons: A canonical microcircuit for inhibition? *J Neurosci*. 2011;31(37):13260-13271. doi:10.1523/JNEUROSCI.3131-11.2011
5. Fino E, Yuste R. Dense inhibitory connectivity in neocortex. *Neuron*. 2011;69(6):1188-1203. doi:10.1016/j.neuron.2011.02.025
6. Inan M, Blázquez-Llorca L, Merchán-Pérez A, Anderson SA, DeFelipe J, Yuste R. Dense and overlapping innervation of pyramidal neurons by chandelier cells. *J Neurosci*. 2013;33(5):1907-1914. doi:10.1523/JNEUROSCI.4049-12.2013
7. Varga C, Lee SY, Soltesz I. Target-selective GABAergic control of entorhinal cortex output. *Nat Neurosci*. 2010;13(7):822-824. doi:10.1038/nn.2570
8. Lee AT, Gee SM, Vogt D, Patel T, Rubenstein JL, Sohal VS. Pyramidal neurons in prefrontal cortex receive subtype-specific forms of excitation and inhibition. *Neuron*. 2014;81(1):61-68. doi:10.1016/j.neuron.2013.10.031
9. Valero M, Cid E, Averkin RG, et al. Determinants of different deep and superficial CA1 pyramidal cell dynamics during sharp-wave ripples. *Nat Neurosci*. 2015;18(9):1281-1290. doi:10.1038/nn.4074
10. Lu J, Tucciarone J, Padilla-Coreano N, He M, Gordon JA, Josh Huang Z. Selective inhibitory control of pyramidal neuron ensembles and cortical subnetworks by chandelier cells. *Nat Neurosci*. 2017;20(10):1377-1383. doi:10.1038/nn.4624
11. Liu X, Dimidschstein J, Fishell G, Carter AG. Hippocampal inputs engage CCK+ interneurons to mediate endocannabinoid-modulated feed-forward inhibition in the prefrontal cortex. *Elife*. 2020;9. doi:10.7554/elife.55267
12. Wu SJ, Sevier E, Dwivedi D, et al. Cortical somatostatin interneuron subtypes form

cell-type-specific circuits. *Neuron*. 2023:1-18. doi:10.1016/j.neuron.2023.05.032

13. Krook-Magnuson E, Varga C, Lee SH, Soltesz I. New dimensions of interneuronal specialization unmasked by principal cell heterogeneity. *Trends Neurosci*. 2012;35(3):175-184. doi:10.1016/j.tins.2011.10.005
14. Lee SH, Marchionni I, Bezaire M, et al. Parvalbumin-positive basket cells differentiate among hippocampal pyramidal cells. *Neuron*. 2014;82(5):1129-1144. doi:10.1016/j.neuron.2014.03.034
15. Foldy C, Lee SY, Szabadics J, Neu A, Soltesz I. Cell type–specific gating of perisomatic inhibition by cholecystokinin. *Nat Neurosci*. 2007;10. doi:10.1016/j.neuron.2013.07.001
16. Hattox AM, Nelson SB. Layer V neurons in mouse cortex projecting to different targets have distinct physiological properties. *J Neurophysiol*. 2007;98(6):3330-3340. doi:10.1152/jn.00397.2007
17. Brown SP, Hestrin S. Intracortical circuits of pyramidal neurons reflect their long-range axonal targets. *Nature*. 2009;457(7233):1133-1136. doi:10.1038/nature07658
18. Kim EJ, Juavinett AL, Kyubwa EM, Jacobs MW, Callaway EM. Three Types of Cortical Layer 5 Neurons That Differ in Brain-wide Connectivity and Function. *Neuron*. 2015;88(6):1253-1267. doi:10.1016/j.neuron.2015.11.002
19. Molnár Z, Cheung AFP. Towards the classification of subpopulations of layer V pyramidal projection neurons. *Neurosci Res*. 2006;55(2):105-115. doi:10.1016/j.neures.2006.02.008
20. Morishima M, Morita K, Kubota Y, Kawaguchi Y. Highly differentiated projection-specific cortical subnetworks. *J Neurosci*. 2011;31(28):10380-10391. doi:10.1523/JNEUROSCI.0772-11.2011
21. Klausberger T, Somogyi P. Neuronal diversity and temporal dynamics: The unity of hippocampal circuit operations. *Science (80-)*. 2008;321(5885):53-57. doi:10.1126/science.1149381
22. Freund TF, Katona I. Perisomatic Inhibition. *Neuron*. 2007;56(1):33-42. doi:10.1016/j.neuron.2007.09.012
23. Sommeijer JP, Levelt CN. Synaptotagmin-2 is a reliable marker for parvalbumin positive inhibitory boutons in the mouse visual cortex. *PLoS One*. 2012;7(4):1-12. doi:10.1371/journal.pone.0035323
24. Katona I, Sperlagh B, Sik A, et al. Presynaptically Located CB1 Cannabinoid

Receptors Regulate GABA Release from Axon Terminals of Specific Hippocampal interneurons. *J Neurosci*. 1999;19(11):4544-4558.

25. Takács VT, Szőnyi A, Freund TF, Nyiri G, Gulyás AI. Quantitative ultrastructural analysis of basket and axo-axonic cell terminals in the mouse hippocampus. *Brain Struct Funct*. 2015;220(2):919-940. doi:10.1007/s00429-013-0692-6
26. Klingler E, De la Rossa A, Fièvre S, Devaraju K, Abe P, Jabaudon D. A Translaminar Genetic Logic for the Circuit Identity of Intracortically Projecting Neurons. *Curr Biol*. 2019;29(2):332-339.e5. doi:10.1016/j.cub.2018.11.071
27. Molyneaux BJ, Goff LA, Brettler AC, et al. DeCoN: Genome-wide analysis of invivo transcriptional dynamics during pyramidal neuron fate selection in neocortex. *Neuron*. 2015;85(2):275-288. doi:10.1016/j.neuron.2014.12.024
28. Sanes JR, Zipursky SL. Synaptic Specificity, Recognition Molecules, and Assembly of Neural Circuits. *Cell*. 2020;181(3):536-556. doi:10.1016/j.cell.2020.04.008
29. Südhof TC. Towards an Understanding of Synapse Formation. *Neuron*. 2018;100(2):276-293. doi:10.1016/j.neuron.2018.09.040
30. De Wit J, Ghosh A. Specification of synaptic connectivity by cell surface interactions. *Nat Rev Neurosci*. 2016;17(1):22-35. doi:10.1038/nrn.2015.3
31. Shen K, Scheiffele P. Genetics and Cell Biology of Building Specific Synaptic Connectivity. *Annu Rev Neurosci*. 2010;33:473-509. doi:10.1146/annurev.neuro.051508.135302
32. Favuzzi E, Deogracias R, Marques-Smith A, et al. Distinct molecular programs regulate synapse specificity in cortical inhibitory circuits_ suppl.data. *Science (80-)*. 2019;363(6425):413-417. doi:10.1126/science.aau8977
33. Gerfen CR, Paletzki R, Heintz N. GENSAT BAC cre-recombinase driver lines to study the functional organization of cerebral cortical and basal ganglia circuits. *Neuron*. 2013;80(6):1368-1383. doi:10.1016/j.neuron.2013.10.016
34. Gouwens NW, Sorensen SA, Baftizadeh F, et al. Integrated Morphoelectric and Transcriptomic Classification of Cortical GABAergic Cells. *Cell*. 2020:935-953. doi:10.1016/j.cell.2020.09.057
35. Osakada F, Callaway EM. Design and generation of recombinant rabies virus vectors. *Nat Protoc*. 2013;8(8):1583-1601. doi:10.1038/nprot.2013.094
36. Suzuki T, Morimoto N, Akaike A, Osakada F. Multiplex Neural Circuit Tracing With G-Deleted Rabies Viral Vectors. *Front Neural Circuits*. 2020;13(January):1-23.

doi:10.3389/fncir.2019.00077

37. Lim L, Mi D, Llorca A, Marín O. Development and Functional Diversification of Cortical Interneurons. *Neuron*. 2018;100(2):294-313. doi:10.1016/j.neuron.2018.10.009
38. Fishell G, Kepecs A. Interneuron Types as Attractors and Controllers. *Annu Rev Neurosci*. 2020;43(1):1-30. doi:10.1146/annurev-neuro-070918-050421
39. Fishell G, Rudy B. *Mechanisms of Inhibition within the Telencephalon: "Where the Wild Things Are."* Vol 34.; 2011. doi:10.1146/annurev-neuro-061010-113717
40. Somogyi P, Klausberger T. Defined types of cortical interneurone structure space and spike timing in the hippocampus. *J Physiol*. 2005;562(1):9-26. doi:10.1113/jphysiol.2004.078915
41. Le Bé JV, Silberberg G, Wang Y, Markram H. Morphological, electrophysiological, and synaptic properties of corticocallosal pyramidal cells in the neonatal rat neocortex. *Cereb Cortex*. 2007;17(9):2204-2213. doi:10.1093/cercor/bhl127
42. Strüber M, Jonas P, Bartos M. Strength and duration of perisomatic GABAergic inhibition depend on distance between synaptically connected cells. *Proc Natl Acad Sci U S A*. 2014. doi:10.1073/pnas.1412996112
43. Ciatto C, Bahna F, Zampieri N, et al. T-cadherin structures reveal a novel adhesive binding mechanism. *Nat Publ Gr*. 2010;17(3):25-28. doi:10.1038/nsmb.1781
44. Brasch J, Katsamba PS, Harrison OJ, et al. Homophilic and Heterophilic Interactions of Type II Cadherins Identify Specificity Groups Underlying Cell-Adhesive Behavior. *Cell Rep*. 2018;23(6):1840-1852. doi:10.1016/j.celrep.2018.04.012.Homophilic
45. Wu PR, Cho KKA, Vogt D, Sohal VS, Rubenstein JLR. The cytokine CXCL12 promotes basket interneuron inhibitory synapses in the medial prefrontal cortex. *Cereb Cortex*. 2017;27(9):4303-4313. doi:10.1093/cercor/bhw230
46. Ranscht B, Zimmermann MTD. T-Cadherin , a Novel Cadherin Cell Adhesion Molecule in the Nervous System lacks the Conserved Cytoplasmic Region. *Neuron*. 1991;7.
47. Philippova M, Joshi MB, Kyriakakis E, Pfaff D, Erne P, Resink TJ. A guide and guard : The many faces of T-cadherin. *Cell Signal*. 2009;21(7):1035-1044. doi:10.1016/j.cellsig.2009.01.035
48. Callaway EM, Luo L. Monosynaptic circuit tracing with glycoprotein-deleted rabies viruses. *J Neurosci*. 2015;35(24):8979-8985. doi:10.1523/JNEUROSCI.0409-15.2015

49. Osakada F, Callaway EM. Design and generation of recombinant rabies virus vectors. *Nat Protoc*. 2013. doi:doi:10.1038/nprot.2013.094.
50. Strüber M, Jonas P, Bartos M. Strength and duration of perisomatic gabaergic inhibition depend on distance between synaptically connected cells. *Proc Natl Acad Sci U S A*. 2015;112(4):1220-1225. doi:10.1073/pnas.1412996112
51. Denardo LA, Berns DS, Deloach K, Luo L. Connectivity of mouse somatosensory and prefrontal cortex examined with trans-synaptic tracing. *Nat Neurosci*. 2015;18(11):1687-1697. doi:10.1038/nn.4131
52. Frandolig JE, Matney CJ, Lee K, et al. The Synaptic Organization of Layer 6 Circuits Reveals Inhibition as a Major Output of a Neocortical Sublamina. *Cell Rep*. 2019;28(12):3131-3143.e5. doi:10.1016/j.celrep.2019.08.048
53. Yetman MJ, Washburn E, Hyun JH, et al. Intersectional monosynaptic tracing for dissecting subtype-specific organization of GABAergic interneuron inputs. *Nat Neurosci*. 2019;22(3):492-502. doi:10.1038/s41593-018-0322-y
54. Pluta S, Naka A, Veit J, et al. A direct translaminar inhibitory circuit tunes cortical output. *Nat Neurosci*. 2015;18(11):1631-1640. doi:10.1038/nn.4123
55. Patiño M, Lagos, WillTasic .N, Patne NS, Tasic B, Zeng H, Callaway EM. Single-cell transcriptomic classification of rabies-infected cortical neurons. *Proc Natl Acad Sci U S A*. 2022:1-11. doi:10.1073/pnas.2203677119/-/DCSupplemental.Published
56. Zhang W. Spatially Resolved Proteomic Profiling Uncovers Structural and Functional Regulators of the Axon Initial Segment Wei. *bioRxiv Prepr*. 2023.
57. Armstrong C, Soltesz I. Basket cell dichotomy in microcircuit function. *J Physiol*. 2012;590(4):683-694. doi:10.1113/jphysiol.2011.223669
58. Dudok B, Klein PM, Hwaun E, et al. Alternating sources of perisomatic inhibition during behavior. *Neuron*. 2021;109(6):997-1012.e9. doi:10.1016/j.neuron.2021.01.003
59. Bloodgood BL, Sharma N, Browne HA, Trepman AZ, Greenberg ME. The activity-dependent transcription factor NPAS4 regulates domain-specific inhibition. *Nature*. 2013;503(7474):121-125. doi:10.1038/nature12743
60. Yap EL, Pettit NL, Davis CP, et al. Bidirectional perisomatic inhibitory plasticity of a Fos neuronal network. *Nature*. 2021;590(7844):115-121. doi:10.1038/s41586-020-3031-0
61. Lur G, Vinck MA, Tang L, Cardin JA, Higley MJ. Projection-Specific Visual Feature Encoding by Layer 5 Cortical Subnetworks. *Cell Rep*. 2016;14(11):2538-2545.

doi:10.1016/j.celrep.2016.02.050

62. Bae JA, Baptiste M, Bodor AL, et al. Functional connectomics spanning multiple areas of mouse visual cortex. *bioRxiv*. 2021:2021.07.28.454025. https://doi.org/10.1101/2021.07.28.454025.
63. Heindorf M, Keller GB. ANTIPSYCHOTIC DRUGS SELECTIVELY DECORRELATE LONG-RANGE INTERACTIONS. *bioRxiv*. 2023.
64. Musall S, Sun XR, Mohan H, et al. Pyramidal cell types drive functionally distinct cortical activity patterns during. *Nat Neurosci*. 2023;26(March). doi:10.1038/s41593-022-01245-9
65. Takahashi N, Ebner C, Sigl-glöckner J, Moberg S, Nierwetberg S, Larkum ME. Active dendritic currents gate descending cortical outputs in perception. *Nat Neurosci*. 2020;23. doi:10.1038/s41593-020-0677-8
66. Vendrell-llopis N, Fang C, Qu AJ, et al. Diverse operant control of different motor cortex populations during learning. *Curr Biol*. 2022;32(7):1616-1622.e5. doi:10.1016/j.cub.2022.02.006
67. Moberg S, Takahashi N. Neocortical layer 5 subclasses : From cellular properties to roles in behavior. 2022;5(October):1-12. doi:10.3389/fnsyn.2022.1006773
68. Dembrow NC, Chitwood RA, Johnston D. Projection-specific neuromodulation of medial prefrontal cortex neurons. *J Neurosci*. 2010;30(50):16922-16937. doi:10.1523/JNEUROSCI.3644-10.2010
69. Exposito-Alonso D, Rico B. Mechanisms Underlying Circuit Dysfunction in Neurodevelopmental Disorders. *Annu Rev Genet*. 2022;56:391-422.
70. Willsey AJ, Sanders SJ, Li M, et al. Coexpression Networks Implicate Human Midfetal Deep Cortical Projection Neurons in the Pathogenesis of Autism. *Cell*. 2013;155(5):997-1007. doi:10.1016/j.cell.2013.10.020
71. Munz M, Bharioke A, Kosche G, et al. Article Pyramidal neurons form active , transient , multilayered circuits perturbed by autism- associated mutations at the inception of neocortex ll ll Article Pyramidal neurons form active , transient , multilayered circuits perturbed by autism- associat. *Cell*. 2023;186:1930-1949. doi:10.1016/j.cell.2023.03.025
72. Goebbels S, Bormuth I, Bode U, Hermanson O, Schwab MH. Genetic Targeting of Principal Neurons in Neocortex and Hippocampus of NEX-Cre Mice. 2006;621:611-621. doi:10.1002/dvg

73. Miyamichi K, Amat F, Moussavi F, et al. Cortical representations of olfactory input by trans-synaptic tracing. *Nature*. 2011;472(7342):191-199. doi:10.1038/nature09714
74. Paxinos G. *Atlas of the Developing Mouse Brain at E17.5, P0 and P6*. Elsevier Science; 2007. https://books.google.co.uk/books?id=zCxBslzi1VkC.
75. Paxinos G, Franklin KB. Atlas of the Adult Mouse brain. 2004.
76. Wu YE, Pan L, Zuo Y, Li X, Hong W. Detecting Activated Cell Populations Using Single-Cell RNA-Seq. *Neuron*. 2017;96(2):313-329.e6. doi:10.1016/j.neuron.2017.09.026
77. Molyneaux BJ, Goff LA, Brettler AC, et al. DeCoN: Genome-wide analysis of invivo transcriptional dynamics during pyramidal neuron fate selection in neocortex. *Neuron*. 2015;85(2):275-288. doi:10.1016/j.neuron.2014.12.024
78. De Wit J, Ghosh A. Specification of synaptic connectivity by cell surface interactions. *Nat Rev Neurosci*. 2016;17(1):22-35. doi:10.1038/nrn.2015.3
79. de Wit J, Hong W, Luo L, Ghosh A. Role of Leucine-Rich Repeat Proteins in the Development and Function of Neural Circuits. *Annu Rev Cell Dev Biol*. 2011;27(1):697-729. doi:10.1146/annurev-cellbio-092910-154111
80. Klingler E, De la Rossa A, Fièvre S, Devaraju K, Abe P, Jabaudon D. A Translaminar Genetic Logic for the Circuit Identity of Intracortically Projecting Neurons. *Curr Biol*. 2019;29(2):332-339.e5. doi:10.1016/j.cub.2018.11.071
81. Yao Z, van Velthoven CTJ, Nguyen TN, et al. A taxonomy of transcriptomic cell types across the isocortex and hippocampal formation. *Cell*. 2021;184(12):3222-3241.e26. doi:10.1016/j.cell.2021.04.021

EXPERIMENTAL MODEL AND SUBJECT DETAIL

Animals

Tlx3^{Cre} [33] and *Nex*^{Cre} [72] were maintained in a C57BL/6 background (Charles River Laboratories). Animals were housed in groups of up to five littermates and maintained under standard, temperature controlled, laboratory conditions. Mice were kept on a 12:12 light/dark cycle and received water and food *ad libitum*. All animal procedures were approved by the ethical committee (King's College London) and conducted in accordance with European regulations, and Home Office personal and project licenses under the UK Animals (Scientific Procedures) 1986 Act.

METHOD DETAILS

Plasmids design

shRNA

Cdh12 and *Cdh13 shRNA* were cloned into a *pAAV-EF1a-DIO-mCherry* vector as previously described [32]. The ssDNA primers to generate the *shRNAs* were obtained using the Block-it RNAi web tool (Thermo Scientific) and were as follows: *shCdh12#1* (Fwd: CTA GGC ATT CGG ACT TGG ATA AAG GCC TGA CCC ACC TTT ATC CAA GTC CGA ATG CTT TTTG and Rev: AAT TCA AAA AGC ATT CGG ACT TGG ATA AAG GTG GGT CAG GCC TTT ATC CAA GTC CGA ATGC); *shCdh12#2* (Fwd: CTA GGC AGT ACC AGG TCC TCA TTC ACC TGA CCC ATG AAT GAG GAC CTG GTA CTG CTT TTTG and Rev: AAT TCA AAA AGC AGT ACC AGG TCC TCA TTC ATG GGT CAG GTG AAT GAG GAC CTG GTA CTGC; *shCdh12#3* (Fwd: CTA GGC TGG GCC ATT TAA GGA TAC TCC TGA CCC AAG TAT CCT TAA ATG GCC CAG CTT TTTG and Rev AAT TCA AAA AGC TGG GCC ATT TAA GGA TAC TTG GGT CAG GAG TAT CCT TAA ATG GCC CAGC); *shCdh12#4* (Fwd: CTA GGC AAT TCT CCT TTA GAT TAG CCC TGA CCC AGC TAA TCT AAA GGA GAA TTG CTT TTTG and Rev: AAT TCA AAA AGC AAT TCT CCT TTA GAT TAG CTG GGT CAG GGC TAA TCT AAA GGA GAA TTGC); *shCdh12#5*

(Fwd: CTA GGC ACG AAT ACA ATG ACTAT TCC CTG ACC CAG AAT AGT CAT TGT ATT CGT GCT TTT TG and Rev: AAT TCA AAA AGC ACG AAT ACA ATG ACT ATT CTG GGT CAG GGA ATA GTC ATT GTA TTC GTGC); *shCdh13*#1 (Fwd: CTA GGC TCC TTG CAG GAT ATC TTT ACC TGA CCC ATA AAG ATA TCC TGC AAG GAG CTT TTTG and AAT TCA AAA AGC TCC TTG CAG GAT ATC TTT ATG GGT CAG GTA AAG ATA TCC TGC AAG GAGC); *shCdh13#2* (Fwd: CTA GGG GCT GCA TAC ACC ATC ATC ACC TGA CCC ATG ATG ATG GTG TAT GCA GCC CTT TTTG and Rev: AAT TCA AAA AGG GCT GCA TAC ACC ATC ATC ATG GGT CAG GTG ATG ATG GTG TAT GCA GCCC); *shCdh13#3* (Fwd: CTA GGC TGA TCA AAG TGG AGA ATG ACC TGA CCC ATC ATT CTC CAC TTT GAT CAG CTT TTTG and Rev: AAT TCA AAA AGC TGA TCA AAG TGG AGA ATG ATG GGT CAG GTC ATT CTC CAC TTT GAT CAGC); *shCdh13#4* (Fwd: CTA GGC CTT CTT CAG AAT CTG AAC ACC TGA CCC ATG TTC AGA TTC TGA AGA AGG CTT TTTG and Rev: AAT TCA AAA AGC CTT CTT CAG AAT CTG AAC ATG GGT CAG GTG TTC AGA TTC TGA AGA AGGC); *shCdh13#5* (Fwd: CTA GGC CCA TCA TGG TGA CAG ATT CCC TGA CCC AGA ATC TGT CAC CAT GAT GGG CTT TTTG and Rev: AAT TCA AAA AGC CCA TCA TGG TGA CAG ATT CTG GGT CAG GGA ATC TGT CAC CAT GAT GGGC). The same *shLacZ* as described in [32] was used as a control condition.

Rabies

Constructs used for the multiplex G-deleted rabies virus-mediated circuit mapping approach were generated by standard molecular biology cloning procedures. The *pSAD ΔG H2B:GFP* was obtained by taking advantage of the *pSAD ΔG F3* expression vector (kindly provided by Dr. M. Tripodi, Cambridge University, AddGene #32634). The nucleotide sequence encoding the histone H2B-tagged GFP was designed and ordered via GeneArts (ThermoFisher

Scientific). Subsequently, it was subcloned within the *pSAD ΔG F3* expression vector by a restriction enzyme-based method, using the unique restriction enzymes AscII and BsiWI (New England Bioscience). The membrane-bound *EGFP::T2A::TVA* cassette was obtained by gene synthesis. A DNA fragment containing the nucleotide sequence of the membrane-bound EGFP link via a T2A cleaving site to the coding sequence of TVA^{TC66} receptor [73] was designed in an inverted orientation and ordered via GeneArts (ThermoFisher Scientific). This DNA sequence was subsequently amplified by Q5 Hot Start High Fidelity DNA polymerase-based PCR (New England Bioscience) using primers containing the unique restriction sites AccI and NheI (Fwd: TAA GCA GTC GAC TTA CTT GGA TGC GCT TTC AAG and Rev: TGC TTA GCT AGC GCC ACC ATG CTG TGC TGT ATG). The amplified sequence was then inserted within the expression vector *pAAV-hSyn-fDIO-MCS* (kindly provided by Dr. M. Selten and Dr. O. Marín) using the AccI and NheI sites.

The same experimental approach has been used to generate the *pAAV-hSyn fDIO oG* expression vector. The oG nucleotide sequence was PCR amplified using specific primers containing the restriction sites AccI and NheI (Fwd: TAA GCA GTC GAC TTA GAG CCG TGT CTC GCC and Rev: TGC TTA GCT AGC GCC ACC ATG GTC CCA CAG GCT CTC CTC) and then cloned into *pAAV-hSyn-fDIO-MCS*. The *pAAV-TVB-tagBFP::T2A::oG* was designed as previously described [36] and ordered via GeneArts (ThermoFisher Scientific). The cassette was then sub-cloned into the expression vector *pAAV-hSyn Flex tdTomato::T2A::SypEGFP* (AddGene #51509) using the AscI and FseI restriction sites. All constructs were verified by sequencing.

Cell culture and transfection

HEK293T cells were cultured in Dulbecco's Modified Eagle's medium supplemented with 10% fetal bovine serum, 2 mM glutamine, penicillin (50 units/ml) and streptomycin (50 g/ml).

The cultures were incubated at 37°C in a humidified atmosphere containing 5% CO_2. HEK293T cells were transfected using polyethylenimine (PEI, Sigma) at a 1:4 DNA:PEI ratio or Lipofectamine 2000 (Thermo Fisher Scientific).

AAV and rAAVretro production

HEK293FT cells (Thermo Fisher Scientific) were seeded on 15-cm plates and co-transfected with packaging plasmids AAV-ITR-2 genomic vectors (7.5 μg), AAV-Cap8 vector pDP8 (30 μg; PlasmidFactory GmbH, Germany, #pF478) or AAV-Cap DJ Rep-Cap vector (30 μg; Cell Biolabs, VPK-420-DJ) using PEI (Sigma) at a ratio 1:4 (DNA:PEI). 72 hours post-transfection, supernatants were incubated with Ammonium sulfate (65g/200ml supernatant) for 30 minutes on ice and centrifuged for 45 minutes at 4000 RPM at 4°C. Transfected cells were harvested and lysed (150mM NaCl, 50mM Tris pH8.5), followed by three freeze-thaw cycles and Benzonase treatment (50U/ml; Sigma) for 1 hour at 37°C. Filtered AAVs (0.8 μm and 0.45 μm MCE filters) from supernatants and lysates were run on an Iodixanol gradient by ultracentrifugation (Vti50 rotor, Beckmann Coultier) at 50,000 RPM for 1 hour at 12°C. The 40% iodixanol fraction containing the AAVs was collected, concentrated using 100 kDa-MWCO Centricon plus-20 and Centricon plus-2 (Merck-Millipore), aliquoted and stored at -80°C. The number of genomic copies was determined by qPCR using the following primers against the WPRE (Fwd: GGC ACT GAC AAT TCC GTG GT and Rev: CGC TGG ATT GAG GGC CGAA). AAVs with a titer equal or higher to 10^{12} genome copy/ml were used for *in vivo* injections. For down-regulation experiments, the two shRNAs with the most efficient down-regulation *in vitro* were used for each target gene. The two shRNA plasmids were co-transfected for AAV production in order to increase the down-regulation efficiency.

Rabies production

Cell lines

HEK-TVA (The Salk Institute of Biological Sciences), HEK-TVB (The Salk Institute of Biological Sciences), BHK-EnvA (kindly gift from Dr. T. Karayannis, University of Zurich), BHK- EnvB (The Salk Institute of Biological Sciences), and B7GG (kind gift from Dr. T. Karayannis) cells were maintained in DMEM (Gibco), supplemented with 10% fetal bovine serum (FBS) in a humified atmosphere of 3% CO_2 and 35°C.

G-deleted rabies virus production

G-deleted rabies viruses (RVΔG) were produced as previously described [49]. Briefly, *RVΔG-H2B:GFP* and *RVΔG-tdTomato* were recovered in B7GG cells by Lipofectamine 2000 (Thermo Fisher Scientific) transfection with *pcDNA-SADB19N*, *pcDNA-SADB19P*, *pcDNA-SADB19L* and *pSADΔG H2B:GF*P or *pSADΔG:tdTomato*. During the virus production, the transfected cells were maintained using DMEM medium (Gibco) supplemented with 10% FBS in a humified atmosphere of 3% CO_2 and 35°C.

For pseudotyping with EnvA and EnvB, BHK-EnvA and BHK-EnvB cell lines were infected with unpseudotyped *SAD ΔGtdTomato* and *SAD ΔGH2B:GFP* rabies viruses, respectively. Subsequently, infected cells were washed with PBS, collected by 0.25% trypsin-EDTA and replated in new dishes. The virus-containing medium was then filtrated via 0.45-μm filters (Cornings) and concentrated through two rounds of ultra-centrifugation. The infectious titers of the purified viruses were determined using the HEK-TVA and HEK-TVB cell lines. In addition, the presence of any contamination of unpseudotyped rabies virus was detected by using HEK293T cells. Aliquots containing pseudotyped rabies viruses were stored at -80C.

Stereotaxic Injections

Retrobeads

L5 pyramidal cell subpopulations were retrogradely labelled using green (488nm) or red (555nm) fluorescent retrobeads IX (Lumafluor Corp., FL). P2-3 pups were anesthetized with isoflurane and mounted on a stereotactic frame using a 3D printed isoflurane mask. Unilateral injections of 75nl retrobeads at 30nl/min were carried out as follows. L5 IT were labelled by targeting the contralateral somatosensory cortex (S1) (AP +1.6, ML -1.9 to -2.2, DV -0.8 to -0.5), L5 ET were labelled by targeting the Pons (AP -0.3, ML +0.3, DV -4.5 to -4.0). Retrobeads were undiluted and sonicated prior to each injection to avoid aggregate formation. The pipette was retracted from the brain after 2min to allow for diffusion.

AAV Viral injections

For i*n situ* hybridization experiments, we followed the same experimental design as previously described to target L5 IT and L5 ET subpopulations. Briefly, 300nl of *rAAV2retro-Ef1a-tagBFP* (1,02.10^{12} vg/ml) and 300nl of *rAAV2retro-Ef1a-NLS-tdTomato* (4,82.10^{12} vg/ml) were injected at 60nl/min in the contralateral S1 and ipsilateral Pons of P2/3 WT pups.
For *Cdh12* and *Cdh13* down-regulation experiments, we injected 300nl of *AAV8-Ef1a-DIO-shCdh12-mCherry* (8,20.1^{11} vg/ml) or *AAV8-Ef1a-DIO-shCdh13-mCherry* (9,1.10^{11} vg/ml) or *AAV8-DIO-shLacZ-mCherry* (1,20.10^{12} vg/ml) in the S1 of P2/3 pups. *Tlx3-Cre* mice were used to specifically access L5 IT, while L5 ET were specifically targeted by injecting 300nl of *rAAV2retro-Cre* (AddGene, 2.10^{13} vg/ml) in the Pons. The stereotaxic coordinates for the different target areas were the same as for the retrobeads experiment.

Rabies stereotaxic injections

P2-3 *Tlx3-Cre* pups were anesthetized with isoflurane and mounted on a stereotactic frame using a 3D-printed isoflurane mask. A unilateral injection of 300nl *rAAV2retro-FlpO* was made

in the Pons (AP -0.3, ML +0.3, DV -4.4 to -4.0) to target L5 ET axons. 200nl of a mix of *AAV8-DIO-oG* (1,65.10^{12} vg/ml) and *AAV8-DIO-hSyn-TVB-BFP* (4,37.10^{13} vg/ml) (2:1 mix ratio), and 200nl of a mix of AAV8-FRT-oG (9,61.10^{13} vg/ml) and *AAV8-FRT-TVA-mGFP* (9,87.10^{13} vg/ml, 2:1 mix ratio) were co-injected in the ipsilateral somatosensory cortex (S1, AP +1.6, ML -1.9 to -2.2, DV -0.8 to -0.5). All viral injections were made at a 60nl/min rate using a Micro2T nanoinjector (WPI). The pipette was retracted from the brain after 5min, and the wound was closed using VetBond glue. Three weeks later, a second injection of 500nl of a mix of *RVΔG-EnvB-H2B:GFP* (1,6.10^{10} TU/ml) and *RVΔG-EnvA-tdTomato* (3,65.10^{8} TU/ml, kind gift from A. Delogu) (1:1 ratio) was made in the ipsilateral S1BF (AP-1.8, ML 3.2, DV -0.7 --> -0.4). After suturing and disinfecting with Betadine, mice received a subcutaneous injection of Buprenorphine (0.03 mg/ml) to prevent acute pain. Note that the stereotaxic coordinates for the different target areas were determined from the lambda in pups (Atlas of the Developing Mouse Brain [74]) and the bregma in young adults [75].

Tissue dissociation and Fluorescence-Activated Cell Sorting (FACS)

P2-3 C57BL/6 mice were injected, as previously described, with Red Retrobeads™ IX (RB555, LumaFluor) either in S1BF to target L5 IT or in the pons to label L5 ET. To isolate individual cells, we euthanized mice at P10, extracted the brain and microdissected lower layers of S1 in cold pH 7.3 dissociation media containing 14mM $MgCl_2$, 2mM HEPES (Invitrogen 15630-106), 0.2mM NaOH (Sigma S0899), 90mM Na_2SO_4 (Sigma S6547), 30mM K_2SO_4 (Sigma P9458), 3.6mg/mL D-(+)-Glucose (Sigma G6152), 0.8mM kynurenic acid (Sigma K3375), 50 μM AP-V (Sigma A5282), 50U/mL penicillin/streptomycin (Thermo Fisher 15140122). To generate single-cell suspensions, 1 mm^3 tissue pieces from 2-3 brains were pooled and enzymatically digested in a dissociation medium containing 0.16 mg/mL cysteine (Sigma C9768), 7 U/mL Papain (Sigma P3125), 0.1mg/mL DNase (Sigma

10104159001) at 37˚C for 30min. Papain digestion was then blocked with a dissociation medium containing 0.1mg/mL ovomucoid (Sigma, St. Louis, MO T2011) and 0.1mg/mL bovine serum albumin (BSA, Sigma A4161) for 1 min at room temperature. Neurons were mechanically dissociated to create a single cell suspension in iced OptiMEM solution containing 3.6mg/mL D-(+)-Glucose, 4 mM $MgCl_2$, 0.4mM kynurenic acid, 25 μM AP-V, 0.04 mg/mL DNase, diluted in OptiMEM medium (Thermo Fisher, #31985). Actinomycin D (Sigma, A1410) was added during the dissociation process to protect the tissue and prevent activation of immediate early genes [76]. Cells were centrifugated at 120g for 5 min at 4˚C, resuspended in 150-300 μL of fresh complemented OptiMEM and passed through a 40 μm cell strainer. Retrobeads-labelled individual cells were then purified from the cell suspension using a BD FACS Aria III cytometer. Cells were collected in 350µl of RLT buffer (RNeasy Lysis buffer, QIAGEN) containing 1% 2-Mercaptoethanol and stored at -80°C for RNA extraction.

RNA-sequencing and differential expression analysis

RNA was extracted using the QIAGEN RNeasy Micro Kit according to the manufacturer's instructions. Library preparation and RNA-seq experiments were performed by the Genomic Unit of the Centre for Genomic Regulation (CRG, Barcelona, Spain). Approximately 10,000-20,000 cells were required to obtain 5-10 ng of total RNA, which served as input for the library preparation using the SMARTer v4 Ultra Low RNA Kit. The Illumina HiSeq 2500 platform was used to sequence libraries to a mean of approximately 100 million mapped 125 base pair paired-end reads per sample. In the RNA-seq experiments, three biological replicates were ascertained for each dataset.

RNA-sequencing data processing

Our dataset (this study) was enriched with L5-specific genes using two other complementary RNA-seq datasets: L5-specific genes at P10 [26] and L5-specific genes at P0 [27]. We used the first dataset as a positive control for L5 cell type-specific gene expression at P10 [26]. The second dataset [27] provides an early gene expression and allowed us to ascertain the "L5 neuronal signature" further. Sequencing files from this study and [77] were QC'ed, genome aligned, and gene expression quantified using Nextflow's RNA-seq pipeline (v3.2). Ensembl's GRCm38 annotation and genomic sequences were used as reference. Gene expression counts data were kindly provided by Dr. D Jabaudon (Geneva University) from [26], and an unpublished dataset of ET cortical spinal cord pyramidal cells. Genes with at least 10 read counts in each sample replicated across all studies were kept. Differential gene expression analysis was performed to identify differentially expressed genes (DEGs) between L5 IT and L5 ET neurons in each study using the R/Bioconductor package DESeq2. Genes that showed a 1.5-fold change in expression and passed the 0.05 Bonferroni-adjusted p-values were labelled as differentially expressed. We selected DEGs from this study that are concordantly regulated in [27]. A similar selection process was performed on DEGs identified from [26], and the union of genes from both datasets were used for downstream analyses.

Gene Ontology analysis

Functional enrichment in gene functions was determined using the R/Bioconductor package ClusterProfiler. The org.Mm.eg.db package containing Gene Ontology terms was used as the database, and a list of stably expressed genes was used as background reference. Terms that passed the 0.05 FDR threshold were annotated as significantly enriched.

Scoring of cell-adhesion molecules

A list of ligand-receptor pairs of cell-surface molecules was manually compiled from previous studies [28,29,78,79] and from the STRING database. Fold-change score of the expression of L5 IT- and L5 ET-specific adhesion molecules were calculated from the expression values from this and [80] studies. Essentially, the fold-difference in mean normalized gene expression between L5 IT and L5 ET subpopulations was calculated and scaled to produce values between 0 and 1. The specificity of the interaction between L5 IT with CCK+ interneurons, and between L5 ET with PV+ interneurons was determined by calculating the enrichment in the gene expression of partner adhesion molecules amongst interneuron subpopulations. Gene expression profiles of single cells from [81] were used for this part of the analysis. CCK+ interneurons were identified in the Mouse Atlas by a high expression of the *Cck* gene and moderate/low expression of the *Pvalb* gene. Essentially, log2 fold-difference in the expression of each receptor in CCK+ or PV+ interneurons was calculated by comparing its expression to other interneuron subpopulations. Receptor genes that are positively enriched in CCK+ or PV+ cells were retained and log2 fold-difference values from each ligand-receptor pair were averaged to give a representative specificity score.

Immunohistochemistry

Animals were deeply anesthetized with sodium pentobarbital by intraperitoneal injection and then transcardially perfused with PBS followed by 4% paraformaldehyde (PFA) in PBS. Dissected brains were post-fixed for 2 h at 4˚C, cryoprotected successively in 15% and 30% sucrose (Sigma-Aldrich, Cat# S0389) in PBS, and finally cut frozen on a sliding microtome (Leica SM2010 R) at 40 μm. Free-floating brain slices were permeabilized with 0.25% Triton X-100 (Sigma-Aldrich, Cat# T8787) in PBS for 1 h at room temperature (RT) and blocked for 2 h in a solution containing 0.3% Triton X-100, 1% serum, and 5% bovine serum albumin (BSA) (Sigma-Aldrich, Cat# A8806) at RT. Brain slices were then incubated overnight at 4˚C

with primary antibodies (see Key Resource table). The next day, the tissue was repeatedly rinsed in PBS and incubated with secondary antibodies (see Key Resource table) for 2 h at RT. All primary and secondary antibodies were diluted in 0.3% Triton X-100, 1% serum and 2% BSA.

For perisomatic inputs quantification, the following primary and secondary antibodies were used: mouse anti-NeuN (1:500), rabbit anti-NeuN (1:500), goat anti-CB1R (1:400), mouse anti-CB1R (1:500), rabbit anti-DsRed (1:500), mouse anti-Syt2 (1:125), chicken anti-GFP (1:1000), rabbit anti-GFP (1:500), donkey anti-rabbit 405 (1:250), donkey anti-goat 488 (1:500), goat anti-mouse IgG2b 555 (1:500), donkey anti-mouse 647 (1:500) and goat anti-mouse IgG2a 647 (1:500).

For mapping of L5 IT and L5 ET monosynaptic inputs, every 3 sections containing somatosensory cortex were used (8 sections per mouse) and incubated with the following primary and secondary antibodies: guinea pig anti-RFP (1:500), rabbit anti-tagRFP (1:250), chicken anti-PV (1:250), goat anti-chicken 405 (1:200), goat anti-guinea pig 555 (1:500) and donkey anti-rabbit 647 (1:500).

Single-molecule fluorescence *in situ* hybridization

P10 WT mice co-injected with *rAAV2-retro-tagBFP* and *rAAv2retro-tdTomato* were perfused as previously described. Brains were post-fixed overnight in 4% PFA in PBS, followed by cryoprotection in 30% sucrose-RNase free PBS, and finally sectioned frozen on a sliding microtome at 30 μm. For down-regulation and overexpression experiments, 40 μm slices from P30 mice were used. Fluorescent *in situ* hybridization on brain slices was performed according to manufacturer's protocol (ACD Bio, RNAscope Multiplex Fluorescent Assay v2, #323110). *Cdh12* (ACD Bio, #842531) and *Cdh13* (ACD Bio, #443251-C3) probes were used and visualized with Opal 520 (Akoya BioScience, FP1487001KT) and Opal 650 (Akoya

BioScience, FP1496001KT). Single-molecule dual-color fluorescent *in situ* hybridization was combined with immunohistochemistry, and the following primary and secondary antibodies were used: chicken anti-GFP (1:500, SySy), rabbit anti-tagRFP (1:100, Evrogen), goat anti-chicken biotin (1:200), Streptavidin 555 (1:400), goat anti-chicken 488 (1:600), goat anti-chicken 568 (1:500, ThermoFisher) and donkey anti-rabbit 405 (1:200, Abcam).

Image acquisition and analysis

For the perisomatic inputs analysis, z-stacks (100 X oil immersion objective, 1.44 NA, 2.2 digital zoom, 0.2 μm step size) of 40 μm brain slices were imaged on an inverted Leica TCS-SP8 confocal maintaining same laser power, photomultiplier gain, pinhole, and detection filter settings (1024x1024, 8 bits) and analyzed with IMARIS 7.5.2 software. The density of perisomatic PV+ and CCK+ inputs was then quantified as follows: 1) all z-stacks were submitted to a background subtraction (13.2 μm) and a Gaussian filter (0.0517 μm) step before analysis; 2) L5 IT and L5 ET NeuN+ somatas positive for retrobeads or viral infection were 3D-reconstructed using the "Create surface" tool; 3) Syt2+ and CB1R+ boutons were detected using the "Spots" tool with a spot diameter (XY filter) of 0.8 and 1.2 μm, respectively; 4) the number of Syt2+ perisomatic boutons was quantified using the "Find spots close to surface" tool (ImarisXT extension) with a 0.4 μm threshold distance applied from the 3D-reconstructed NeuN+ surface. 5) the number of CB1R+ perisomatic boutons was quantified using the "Find spots close to surface" tool (ImarisXT extension) with a 0.8 μm distance threshold applied from the 3D-reconstructed NeuN+ surface.

For the *in situ* hybridization analysis, z-stacks (63X oil immersion objective, 1.4 NA, 2.2 digital zoom, 400 Hz, 1 μm step size) of 30-40 μm brain slices were imaged on an inverted Leica TCS-SP8 confocal (1024x1024 resolution, 16 bits) and analyzed using a custom macro in Fiji (ImageJ). Maximum z-stack projections were used for quantification. Somas of infected

L5 IT and L5 ET neurons were drawn manually to create a mask of the soma surface. Cdh12 and Cdh13 RNA particles were detected automatically based on their intensity threshold, and a mask for each probe was generated using the "Analyze Particles" tool. *Cdh12* and *Cdh13* expression levels were determined as a percentage of the probe area normalized by the soma area.

For the monosynaptic tracing analysis, z-stacks (5 μm step size) were imaged on an inverted Zeiss ApoTome (10 X, 1280x800, 16 bits). For each mouse included in the analysis, 8 slices covering the entire S1 area were imaged, and infected cells were manually quantified using the Cell Counter tool in Fiji (ImageJ). The proportion of starter cells was determined as the number of receptor+/rabies+ cells normalized by the number of receptor+ cells across the 8 slices for both L5 pyramidal neuron subpopulations. The proportion of PV+ L5 IT and L5 ET inputs was determined as the number of PV+ inputs divided by the total number of inputs. The laminar proportion of PV+ inputs among L5 IT, L5 ET and L5 IT/ET inputs was determined as the number of PV+ inputs in each layer divided by the total number of PV+ inputs.

In vitro patch-clamp recordings

Mice were deeply anesthetized with an overdose of sodium pentobarbital and transcardially perfused with 10 mL ice-cold slicing solution containing (in mM): 87 NaCl, 75 sucrose, 26 $NaHCO_3$, 11 glucose, 7 $MgCl_2$, 2.5 KCl, 1.25 NaH_2PO_4 and 0.5 $CaCl_2$, oxygenated with 95% O_2 and 5% CO_2. The brain was quickly removed, and the injected hemisphere was glued to a cutting platform before being submerged in ice-cold slicing solution. 300 μm thick coronal slices containing S1Bf were cut using a vibratome (Leica VT1200S, Wetzlar, Germany) and incubated for 45-60 min at 32°C, and subsequently at room temperature, in the same solution. All salts were purchased from Sigma-Aldrich (St. Louis, MO). Slices were transferred to the recording setup and superfused with recording ACSF containing (in mM) 124 NaCl, 1.25

NaH_2PO_4, 3 KCl, 26 $NaHCO_3$, 10 Glucose, 2 $CaCl_2$, and 1 $MgCl_2$, which was oxygenated with 95% O_2 and 5% CO_2 and heated to 34°C. Pipettes (3–5 MΩ) were made from borosilicate glass capillaries using a PC-10 pipette puller (P10, Narishige, London, UK). Miniature inhibitory postsynaptic currents (mIPSCs) were measured using an intracellular solution containing (in mM) 70 K-gluconate, 70 KCl, 10 Hepes, 4 Mg-ATP, 4 K2-phosphocreatine, and 0.4 GTP, adjusted with KOH to pH 7.3 (±290 mOsm). mIPSC recordings were performed at a holding voltage of -76 mV in the presence of 1 μM tetrodotoxin (TTX, HB1035) 10 μM 2,3-Dioxo-6-nitro-1,2,3,4-tetrahydrobenzo[f]quinoxaline-7-sulfonamide (NBQX, HB0443) and 50 μM D-(–)-2-Amino-5-phosphonopentanoic acid (D-APV, HB0225), all of which were purchased from Hello Bio (Bristol, UK). Recordings were made using a Multiclamp 700B amplifier (Molecular Devices, San Jose, CA). The signal was passed through a Hum Bug Noise Eliminator (Digitimer, Welwyn Garden City, UK), sampled at 10 kHz, and filtered at 3 kHz using a Digidata 1440A (Molecular devices, San Jose, CA). Cells were excluded if the access resistance (Ra) exceeded 30 MΩ. mIPSCs were analyzed using MiniAnalysis (SynaptoSoft, Decatur, GA, USA).

Western blot

For Western blot analysis, HEK293T were rinsed with 1x ice-cold PBS. Samples were homogenized in lysis buffer containing 25 mM Tris-HCl pH 8, 50mM NaCl, 1% Triton X-100, 0.5% sodium deoxycholate, 0.001 % SDS and protease inhibitor cocktail (cOmplete Mini, Roche). Samples were resolved by SDS-PAGE and transferred onto PVDF membranes. Membranes were blocked with 5% Blotting-Grade Blocker (Bio-Rad, #1706404) in TBST (20mM Tris-HCl pH7.5, 150mM NaCl and 0.1% Tween20) for 1 hour and probed with the following primary antibodies overnight at 4°C: rabbit anti-actin (1:1000) and mouse anti-HA (1:500, Thermo Fisher). After incubation with HRP-conjugated secondary antibodies (see Key

Resource Table), protein levels were visualized by chemiluminescence. Blots were scanned using a LI-COR Odyssey® Fc Imaging System.

Statistical analysis

All statistical analyses were performed using GraphPad Prism 9 (GraphPad Software). Unless otherwise stated, parametric data were analyzed by *t*-test or one-way ANOVA followed by Holm-Sidak or Tukey *post hoc* analysis for comparisons of multiple samples. Non-parametric data were analyzed by the Mann-Whitney test, multiple t-test or Kruskal-Wallis one-way analysis followed by Holm-Sidak or Dunn *post hoc* analysis for comparisons of multiple samples. P values <0.05 were considered statistically significant. All data are presented as mean ± SEM.